Short-wavelength instabilities on coastal jets and fronts

J. A. Barth

College of Oceanic and Atmospheric Sciences, Oregon State University, Corvallis

Abstract. The stability of a coastal jet and front is investigated using the primitive equations applied to a continuously stratified flow in geostrophic balance. A linear stability analysis successfully explains the growth of two modes of instability with distinctly different horizontal scales. A long-wavelength mode (fastest-growing wavelength of $O(100$ km$)$) is found which is a modified version of a traditional baroclinic instability. A second, rapidly growing frontal instability also exists. For a realistic basic state density and flow structure, this mode has its fastest growth at short wavelengths ($O(20$ km$)$), e-folds in less than 1.5 days and propagates rapidly in the direction of the mean flow. The frontal instability grows primarily by extracting the available potential energy of the mean flow via a baroclinic instability mechanism. A small contribution from vertical Reynolds stress is also found, but the transfer via horizontal Reynolds stress is from the eddy to the mean kinetic energy. Further evidence shows that the frontal instability is not a result of horizontal shear instability nor is it an inertial instability. The frontal mode is trapped to the surface front and its influence is confined to the upper water column ($z \lesssim 70$ m). A significant subsurface vertical velocity maximum (20 m d^{-1} at 30 m) is associated with a frontal instability with a reasonable, as judged by satellite sea surface temperature observations, surface temperature perturbation of 0.35°C. The linear stability predictions are verified by and compared with results from a time-dependent, three-dimensional, nonlinear ocean circulation model. Finally, the frontal instability is discussed in the context of other recent stability analyses that yield high-wavenumber modes.

1. Introduction

Fronts are common and important features of the circulation over the continental shelf and slope. They manifest themselves as sharp horizontal contrasts in temperature, salinity, density, velocity, biologically important nutrients, and in the biology fields themselves. Of particular interest from a dynamical point of view are density fronts and the accompanying along-front jets via the thermal wind balance. Density fronts in the coastal ocean arise from a variety of physical mechanisms, for example, negative or positive buoyancy input, juxtaposition of distinct shelf and slope water masses, and wind-driven coastal upwelling. While each of the resulting density structures is unique, they all share the common feature that a good deal of along-front variability is associated with the surface fronts. Examples of this variability are evident in the buoyancy-driven Norwegian Coastal Current [*Johannessen et al.*, 1989], the shelf/slope front in the Middle Atlantic Bight [*Garvine et al.*, 1988] and a number of coastal upwelling fronts

[*Barth*, 1989b]. The focus of the present investigation will be on coastal upwelling fronts and their accompanying jets. In a broader sense these fronts and jets are an important part of the observed circulation in eastern boundary regions (e.g, off the west coast of the United States [*Strub et al.*, 1991]; off the Iberian peninsula [*Haynes et al.*, 1993]; and off southwestern Africa [*Lutjeharms et al.*, 1991]). Although the dynamical processes discussed in this study are universal, observations from off the west coast of the United States, both over the continental shelf and in the coastal transition zone offshore of the shelf, serve as motivation.

One feature immediately apparent from examining satellite infrared sea surface temperature (SST) maps from off the U.S. west coast during the spring-summer upwelling season (see the recent compilation by *Strub et al.* [1991]), is the mixture of scales of along-front variability on the boundary between cold, nutrient-rich, recently upwelled water inshore and the warmer water offshore. On the largest scale there exist meanders with along-front spacings of roughly 200 km. There appears to be some correspondence between this spacing and the distance between the various capes and points along the coast of southern Oregon and northern California. Model studies of the perturbation of a baroclinically unstable alongshore jet by coastline promontories

[Ikeda and Emery, 1984; *Haidvogel et al.,* 1991a], yield meanders with scales close to those observed. Other recent studies [*McCreary et al.,* 1991; *Allen et al.,* 1991] of similar alongshore baroclinic jets produce large-scale meanders (~ 250 km alongshore spatial scale) without the presence of coastal capes or bottom topographic features.

On an intermediate scale, wavelike meanders with along-front wavelengths of 80–100 km are found on existing offshore jets. A particularly good example is documented by *Swenson et al.* [1992] (see their Figures 6 and 7), where a train of three or four wavelike features is readily apparent in both satellite infrared SST images and in the tracks of several surface drifters which follow the meandering jet. As will be shown below, growing perturbations with this scale are consistent with traditional baroclinic instability.

On an even finer scale, satellite SST images from off the U.S. west coast during the upwelling season reveal the presence of short-scale meanders (~ 20-km wavelengths) on many frontal boundaries. These wavelike perturbations are fairly common and appear to grow rapidly and propagate swiftly in the direction of the mean jet. One example appears as a wave train in a satellite SST image of the coastal upwelling front and

jet off central and southern Oregon (Figure 1a). At least 10 regularly spaced waves are identifiable with an average wavelength of approximately 17 km. When the spatially averaged (cosine filter with a width of 20 km) temperature field is removed, the short-wavelength perturbations appear as cold (white) and warm (black) bands with maximum SST anomalies of 0.35°C (Figure 1b). These small-scale instabilities have also been observed on upwelling fronts and jets in other coastal regions (e.g., off the Iberian peninsula [*Haynes et al.,* 1993]) and on buoyancy-driven coastal currents (e.g., in the Alaska Coastal Current [*Ahlnäs et al.,* 1987] and in the Algerian Current [*Arnone and La Violette,* 1986]).

The goal of the present work is to analyze the stability of a coastal upwelling front and jet in an effort to explain the growth of both the small-scale perturbations and the meanders of larger scale. Since the horizontal shears in these jets can be of the same order as the Coriolis parameter [*Paduan and Niiler,* 1990] and subsurface isopycnals rise to contact the sea surface, traditional quasi-geostrophic stability theory is inappropriate. An analysis based on the full primitive equations will be used here.

Several studies using single-layer (reduced gravity) and two-layer models for the density stratification have
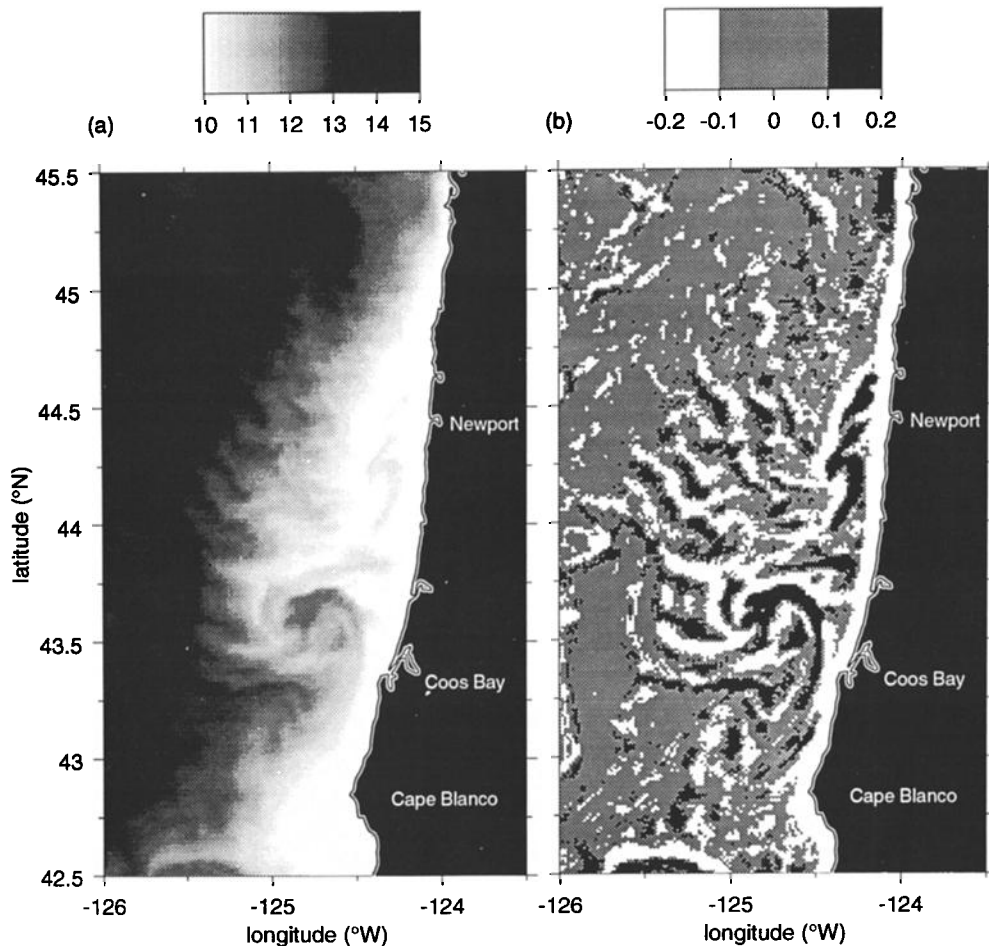
Figure 1. (a) Satellite infrared sea surface temperature (°C) from June 2, 1992, off Oregon. (b) SST anomalies (°C).

yielded insight into the linear instability of various types of fronts [e.g., *Killworth et al.*, 1984 and references therein; *Barth*, 1989a,b; *Paldor and Ghil*, 1991]. As described below, this study will use continuous density stratification to model the coastal front and jet. The present analysis is akin to that carried out by *Moore and Peltier* [1987] in their study of cyclogenesis in atmospheric frontal zones and to the study of the Gulf Stream by *Xue and Mellor* [1993]. *McCreary et al.* [1991] have studied instabilities with both long and short scales in an eastern boundary current using a layered nonlinear, time-dependent numerical model with the uppermost layer being mixed but capable of forming horizontal density contrasts. Recently, Y. Fukamachi et al. (Instability of density fronts in layer and continuously stratified models, submitted to *Journal of Geophysical Research*, 1994) (hereinafter referred to as Fukamachi et al. submitted paper, 1994) have discussed ageostrophic baroclinic instabilities using a 1 1/2-layer and a continuously stratified model, both of which have a constant depth upper layer capable of supporting horizontal temperature gradients.

The outline of this paper is as follows: First, the linear stability analysis technique for a continuously stratified flow using the primitive equations is described. Results for a basic case based on an observed front and jet are presented next. Then, several variations of the basic case are considered, including a brief discussion of the possibility of inertial instability in these highly sheared flows. To verify the linear stability predictions, results from the early stages of a nonlinear, time-dependent, high-resolution numerical model based on the primitive equations are presented. Finally, conclusions are set forth and avenues for future research are discussed.

2. Linear Stability Using the Primitive Equations

For coastal fronts and jets the Rossby number and changes in isopycnal depths and/or bottom topography can be large, making the use of the quasi-geostrophic approximation inappropriate. In this study, the primitive equations, Navier-Stokes equations together with the Boussinesq and hydrostatic approximations, will be used. Rather than modeling the vertical density structure as a number of homogeneous layers separated by sharp interfaces as in other recent studies [e.g., *Killworth et al.*, 1984; *Barth*, 1989a,b], a continuously stratified model is used here. This allows for realistic density stratification, including vertical density variations below the strong pycnocline that may play a role in shielding upper ocean fronts and jets from the influence of bottom topography.

The inviscid, adiabatic primitive equations on an f plane (f is the Coriolis parameter) in Cartesian coordinates (x, y, z) are

$$u_t + \mathbf{u} \cdot \nabla u - fv = -\pi_x \qquad (1a)$$

$$v_t + \mathbf{u} \cdot \nabla v + fu = -\pi_y \qquad (1b)$$

$$0 = -\pi_z + b \qquad (1c)$$

$$u_x + v_y + w_z = 0 \qquad (1d)$$

$$b_t + \mathbf{u} \cdot \nabla b = 0, \qquad (1e)$$

where

$$\mathbf{u} \cdot \nabla = u\frac{\partial}{\partial x} + v\frac{\partial}{\partial y} + w\frac{\partial}{\partial z} \qquad (1f)$$

and subscripts denote partial differentiation. The pressure per unit density is π, and $b = -g\rho/\rho_0$ is the buoyancy, otherwise the notation is standard. The growth of perturbations on a two-dimensional, basic state flow $V(x, z)$ in thermal wind balance with a background density (buoyancy) field $B(x, z)$,

$$fV_z = B_x, \qquad (2)$$

will be studied. Note that B_z is the Brunt-Väisälä frequency and B_x is its horizontal analog.

After linearizing the governing equations, (1), about the basic state, solutions for the three-dimensional perturbations (denoted by primes) are sought in the form of normal modes

$$(u', w') = Re\left[(\hat{u}, \hat{w})e^{i(\sigma t + \ell y)}\right] \qquad (3a)$$

$$(v', \pi', b') = Re\left[i(\hat{v}, \hat{\pi}, \hat{b})e^{i(\sigma t + \ell y)}\right] \qquad (3b)$$

where $Re[\ \ ]$ denotes the real part of the expression in square brackets. The perturbation structures, denoted by circumflexes, are functions of x and z, ℓ is the along-front wavenumber and σ is the (complex) frequency. The resulting equations for the perturbation structures are (dropping circumflexes)

$$(\sigma + \ell V)u - fv = -\pi_x \qquad (4a)$$

$$(\sigma + \ell V)v - wV_z - (f + V_x)u = -\ell\pi \qquad (4b)$$

$$0 = -\pi_z + b \qquad (4c)$$

$$u_x - \ell v + w_z = 0 \qquad (4d)$$

$$(\sigma + \ell V)b - uB_x - wB_z = 0. \qquad (4e)$$

Now one approach [e.g., *Luther and Bane*, 1985] is to eliminate b between (4c) and (4e), solve for u, v, and w in terms of π, and then substitute into the continuity equation to get one equation in the one unknown π. However, the resulting equation is nonlinear in the eigenvalue and is not immediately solvable by standard numerical techniques. The problem can be made linear in the eigenvalue [see *Barth*, 1987] but not without making the storage requirements for the coefficient matrices impractical. *Luther and Bane* [1985] resort to solving the nonlinear eigenvalue problem by a resonance response technique that does not guarantee finding all the possible solutions at a given along-front wavenumber, although it does allow a particular unstable root, once found, to be tracked through wavenumber space.

Alternatively, the method of *Moore and Peltier* [1987] is followed, the essential elements of which are as follows: Three equations in the three unknowns u, v, and b can be formed by eliminating π and w from (4). Specif-

ically, taking $\partial/\partial z$ of (4a) and substituting $\partial/\partial x$ of (4c) (i.e., forming the thermal wind) yields

$$(\sigma + \ell V)u_z + \ell V_z u - f v_z = -b_x. \qquad (5a)$$

A similar operation on (4b) gives

$$(\sigma + \ell V)v_z + \ell V_z v - u_z V_x - u V_{xz}$$
$$-w_z V_z - w V_{zz} - f u_z = -\ell b,$$

but w_z and w can be substituted for from (4d) and (4e), respectively, to yield

$$(\sigma + \ell V)v_z + \ell V_z v - V_x u_z - V_{xz} u + (u_x - \ell v)V_z$$

$$+ \frac{V_{zz}}{B_z}[uB_x - (\sigma + \ell V)b] - f u_z = -\ell b. \qquad (5b)$$

Now solving for w from (4e), taking $\partial/\partial z$ of the result and substituting into (4d) yields the final equation

$$(\sigma + \ell V)b_z + \ell V_z b - B_x u_z - B_{xz} u + (u_x - \ell v)B_z$$

$$+ \frac{B_{zz}}{B_z}[uB_x - (\sigma + \ell V)b] = 0. \qquad (5c)$$

When the coupled equations (5) are solved numerically they form a standard eigenvalue problem which is linear in the eigenvalue σ.

Now instead of using traditional, second-order finite differences to create an algebraic eigenvalue problem, which again would produce very large coefficient matrices for the number of grid points required to adequately resolve the frontal structure, a spectral technique is used in both the vertical and horizontal directions. The spectral technique offers better resolution and hence more rapid solution convergence than that offered by finite differences given the requirement to keep the coefficient matrices of a manageable size.

The choice of basis functions is dictated by the boundary conditions. In the vertical for a flat bottom case, the vertical velocity is required to vanish at the top ($z = 0$) and bottom ($z = -h$) rigid boundaries

$$w = 0. \qquad (6)$$

To include bottom topography, where the bottom boundary condition at $z = -h(x)$ becomes

$$w = -u\frac{\partial h}{\partial x}, \qquad (7)$$

the system is mapped to bottom-following or sigma coordinates following *Xue and Mellor* [1993]. In the new coordinate system the vertical velocity perpendicular to surfaces of constant sigma is required to vanish at the uppermost and lowermost sigma levels. Therefore an appropriate choice of vertical basis functions allows the dependent variables to be written as

$$[u(x,z), v(x,z)] =$$

$$\sum_{\nu=0}^{\infty} \left[u_\nu(x), v_\nu(x)\right] \cos\left(\frac{\nu\pi z}{h}\right) \qquad (8a)$$

$$[w(x,z), b(x,z)] =$$

$$\sum_{\nu=1}^{\infty} \left[w_\nu(x), b_\nu(x)\right] \sin\left(\frac{\nu\pi z}{h}\right). \qquad (8b)$$

The expansion for w is given solely to illustrate the choice of basis functions; w is not calculated directly in the solution procedure, but rather is diagnosed using (4e). In the horizontal the fluid is contained between solid walls at $x = 0, L$ where the condition of no-normal-flow is applied

$$u = 0. \qquad (9)$$

The structure functions on the right-hand side of (8) are then written as

$$u_\nu(x) = \sum_{\lambda=1}^{\infty} \tilde{u}_{\lambda\nu} \sin\left(\frac{\lambda\pi x}{L}\right) \qquad (10a)$$

$$[v_\nu(x), b_\nu(x)] = \sum_{\lambda=0}^{\infty} \left[\tilde{v}_{\lambda\nu}, \tilde{b}_{\lambda\nu}\right] \cos\left(\frac{\lambda\pi x}{L}\right). \qquad (10b)$$

Substitution of the expansions described by (8) and (10) into the governing equations (5) yields a set of residual equations that are required to be orthogonal to a set of weighting functions. Spectral weighting, in which the weighting functions are the complex conjugates of the corresponding basis functions, is used for the $\tilde{u}$ and $\tilde{v}$ equations. For the $\tilde{b}$ equation an orthogonal collocation method, where the weighting functions are Dirac delta functions at discrete collocation points rather than trigonometric basis functions, is used as described in *Moore and Peltier* [1987]. After applying the weighting scheme and using a simple triangular truncation scheme to truncate the expansions at level N, the three variables ($\tilde{u}$, $\tilde{v}$, $\tilde{b}$) are mapped into a one-dimensional vector **x**. This careful ordering, as detailed by *Moore and Peltier* [1987], is also used to map the matrix coefficients into a single, two-dimensional matrix **E** so that a standard algebraic eigenvalue results

$$\mathbf{Ex} = \sigma\mathbf{x}. \qquad (11)$$

The matrix **E** is a function of the basic state $[V(x,z), B(x,z)]$ and the eigenvalue problem is solved repeatedly for many along-front wavenumbers ℓ using an International Math Subroutine Library (IMSL) routine. For a truncation level of N = 30, it takes 14 megawords of memory and 320 s of CPU time to solve the eigenvalue problem for a single value of the along-front wavenumber on a Cray Y-MP.

Finally, since the solution of (11) for a given along-front wavenumber yields N eigenvalues, a procedure for constructing growth rate and phase speed curves for distinct unstable modes from the large number of (σ, ℓ) pairs is necessary. This was done by assuming that the eigenvalues for a particular mode are a continuous function of the along-front wavenumber. In practice, following the fairly distinct phase speed curves for a given mode allowed identification of its accompanying growth rate curve. In some cases, additional informa-

tion about the mode's energetics (see the following paragraph) helped clear up confusing situations.

For later use in diagnosing the various instability processes, the kinetic and potential energy budgets for the perturbations are

$$(EKE)_t = HRS + VRS + VHF \qquad (12a)$$

$$(EPE)_t = HHF - VHF \qquad (12b)$$

where
eddy kinetic energy

$$EKE = \left(\frac{\overline{u^2 + v^2}}{2}\right) \qquad (12c)$$

eddy potential energy

$$EPE = \frac{1}{B_z}\frac{\overline{b^2}}{2} \qquad (12d)$$

horizontal Reynolds stress

$$HRS = -\overline{uv}V_x \qquad (12e)$$

vertical Reynolds stress

$$VRS = -\overline{wv}V_z \qquad (12f)$$

vertical heat flux

$$VHF = +\overline{wb} \qquad (12g)$$

horizontal heat flux

$$HHF = -\overline{ub}\frac{B_x}{B_z} \qquad (12h)$$

and the overbar is an average over a wavelength in the along-front direction and over the whole domain ($0 \leq x \leq L, -h \leq z \leq 0$).

As noted above, the basic state flow $V(x, z)$ is in thermal wind balance with the basic state density (buoyancy) field $B(x, z)$. In this study the basic state is modeled after observations of a meandering offshore jet off northern California taken as part of the Coastal Transition Zone (CTZ) program in June 1987. Figure 2a shows a vertical section of temperature (proxy for density) and directly measured normal velocity from a cross-jet transect taken near 41.5°N [$Kosro\ et\ al.$, 1991]. The velocity structure is modeled as

$$V(x, z) = v_0 e^{z/z_s} e^{-\left(\frac{x-x_J}{x_d}\right)^2} \qquad (13)$$

where z_s is the e-folding scale of the jet in the vertical,
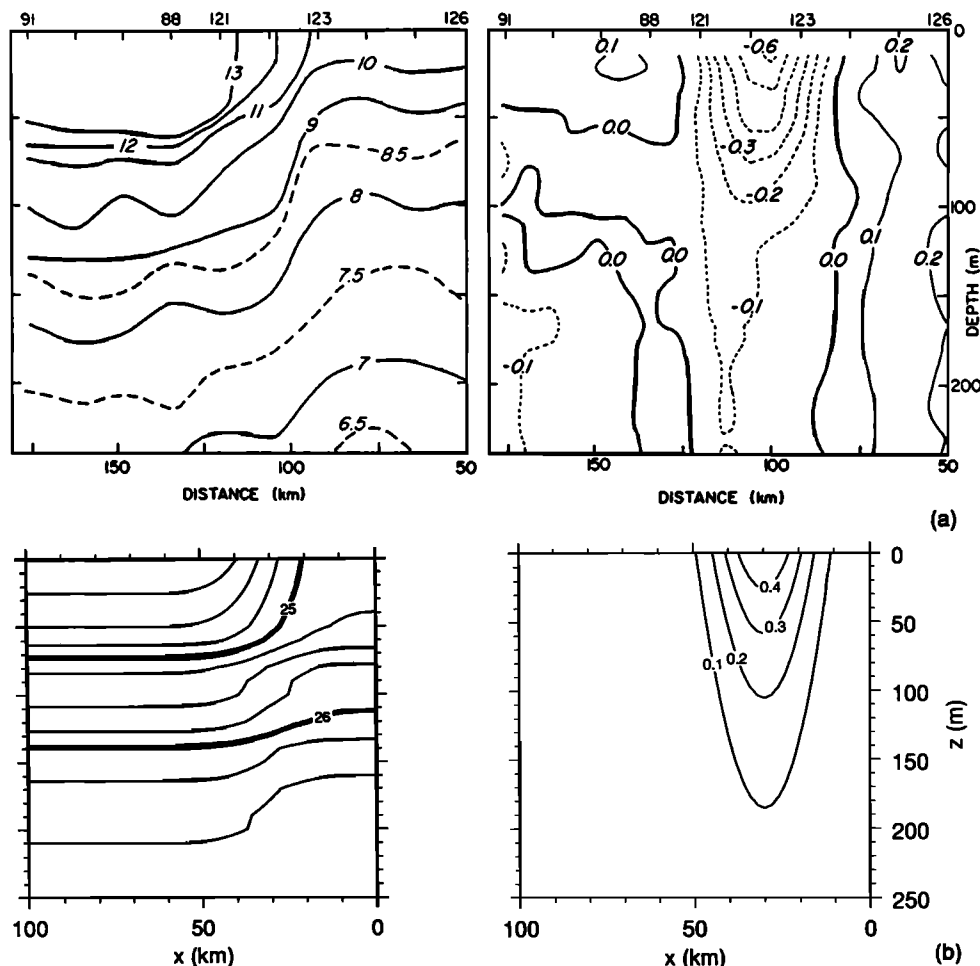
Figure 2. (a) Vertical section of temperature (°C) and directly measured normal velocity (m s^{-1}) from a transect normal to the coast at 41.5°N (data are from $Kosro\ et\ al.$, 1991). (b) Basic state density and velocity (m s^{-1}) structure used in the linear stability analysis.

x_f is the offshore location of the surface front, x_d is the jet's Gaussian half-width and v_0 is the maximum jet speed. To obtain $B(x, z)$, (2) is integrated along constant z levels starting from a vertical profile of density located at the far left of the section shown in Figure 2a, that is, far offshore of the frontal zone. The integration is carried through the frontal zone to the coast ($x = 0$) to obtain the complete density (buoyancy) field.

3. Basic Case

To model the observed velocity and density structure of the CTZ jet near 41.5°N (Figure 2a), the parameters in (13) are chosen to be $v_0 = 0.5$ m s^{-1}, $z_s = 115$ m, $x_d = 15$ km and $x_f = 30$ km. The resulting basic state structure is shown in Figure 2b. The offshore boundary is placed at $x = L = 75$ km, which satisfies the need for sufficient horizontal resolution and the requirement that the unstable modes have negligible amplitude at the offshore wall (see Figure 4 below). The surface front is centered on $x_f = 30$ km, roughly two Rossby radii (R) from the coast using the estimate $R = 15$ km from the density structure shown in Figure 2b. The Rossby radius is obtained from $R = N_{max}H/f$ where $N_{max} = 0.0167$ s^{-1} in the pycnocline that has its base at roughly $H = 90$ m (Figure 2b). *Barth* [1989b] showed that the growth rates of unstable modes on a two-layer upwelling front and jet were relatively insensitive to the proximity of the coastal wall once the surface front was located roughly $2R$ or farther away. Finally, for this case a flat bottom is placed at $h_0 = 250$ m, where the subscript denotes a constant bottom depth, although the real ocean extends to around 3000 m at this particular CTZ jet location. Although a specific CTZ jet transect has been used to motivate this study, the intent here is to examine the stability of a generic coastal upwelling jet which is concentrated in the upper ocean and is typically found over the continental shelf in water of 200 m or less [*Huyer*, 1983]. As will be demonstrated in section 4, changing the bottom depth has virtually no effect on the short-wavelength frontal instability, but does affect the longwave instability in a predictable fashion.

The eigenvalue problem (11) is solved for a range of along-front wavenumbers and the growth rate (σ_i) and phase speed (c_r) curves for two particular modes are shown in Figure 3. These growth rate curves, displayed over a range of wavenumbers, contain the fastest-growing mode at small wavenumbers (solid curves) and at large wavenumbers (dashed curves) from the extensive set of (σ_i, ℓ) solution pairs. The mode with maximum growth rate (e-folding period = 3.56 days) at a wavelength of 92.4 km represents traditional baroclinic instability. This mode will result from a quasi-geostrophic stability analysis [*Pedlosky*, 1987], remembering of course that the quasi-geostrophic basic state will not have isopycnals rising to contact the sea surface. The energy transfer mechanism in this mode (detailed below) is downgradient heat flux as in traditional quasi-geostrophic theory. The wavelength for maximum
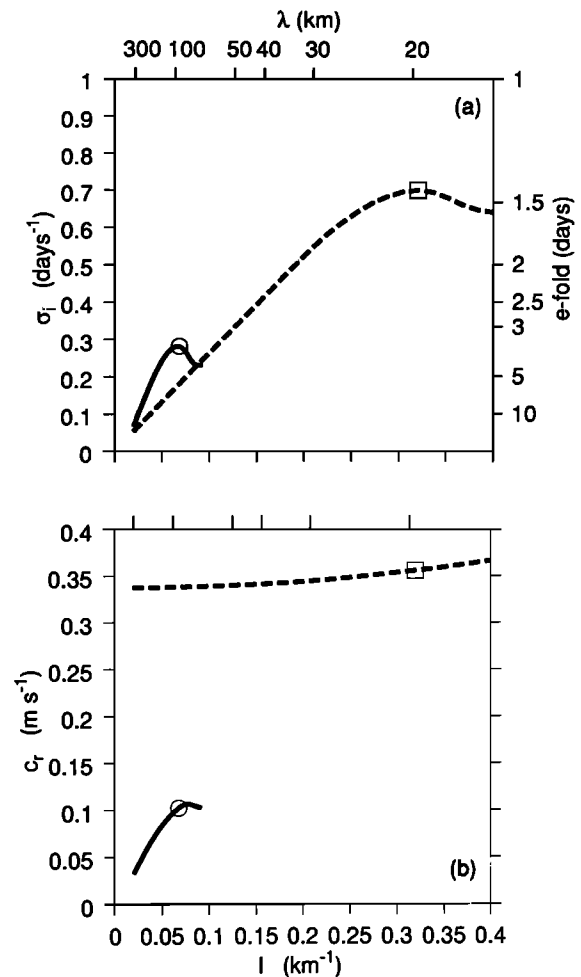
Figure 3. (a) Growth rates and (b) phase speeds for both the traditional baroclinic instability (solid curves) and the frontal instability (dashed curves).

growth corresponds to roughly $2\pi R$, again in agreement with quasi-geostrophic instability theory. At the most unstable wavelength this mode propagates slowly ($c_r = 0.10$ m s^{-1}) in the direction of the basic state flow. This mode of instability on a frontal jet is also discussed by *Samelson* [1993].

The second mode shown in Figure 3 is a form of frontal instability. It has a rapid maximum growth rate (e-folds in 1.43 days) at an along-front wavelength of 19.6 km. This short-wavelength mode is not captured by quasi-geostrophic theory and only appears when the full primitive equations are considered. This type of instability is often called nongeostrophic, or ageostrophic, to distinguish it from conventional geostrophic baroclinic instability. The energy transfer mechanism for the frontal mode (detailed below) is again dominated by the downgradient flux of heat so it represents a form of baroclinic instability. The wavelength of the fastest-growing mode is much closer to the horizontal scale of the basic state horizontal shear ($x_d = 15$ km) than it is to $2\pi R$. The phase speed for the frontal mode is almost independent of wavenumber with the fastest-growing wavelength propagating rapidly ($c_r = 0.36$ m s^{-1}) in

the direction of the basic state flow. The frequency of this fastest-growing wave is close to f.

The results shown in Figure 3 were calculated using 30 polynomials in both the horizontal and vertical directions. Solution convergence was checked by examining the results for $N = 28$. The baroclinic instability model predictions (solid curves, Figure 3) were essentially the same for both truncation levels. For the frontal mode, solution convergence was more sensitive. For $N = 30$ the maximum growth rate was reduced by less than 5% and the accompanying phase speed was less than 2% faster than for the $N = 28$ case. In both cases the maximum growth rate for the frontal model occurred for $\lambda = 19.6$ km, in part because the growth rate curves are relatively flat in this region. Convergence was also tested by comparing the frontal mode structures obtained with the two values of N. Qualitative comparison was excellent and a quantitative measure (absolute difference between the frontal mode's cross-stream velocity magnitude at the surface for different values of N) shows only a few percent difference. Finally, the placement of the offshore boundary at $L = 75$ km is justified by finding satisfactory convergence for the unstable modes by varying N and by the requirement that the proximity of the offshore channel wall not affect the unstable waves' properties as occurs for $L < 75$ km.

To demonstrate further the differences between the two modes, the structures for perturbation cross-stream velocity, along-stream velocity, buoyancy, and vertical velocity for the two modes at their respective fastest-growing wavelengths are shown in Figure 4. The structures for the baroclinic instability mode are centered on x_f, extend deeply into the water column, and are roughly symmetric about x_f. The baroclinic instability mode has an e-folding scale with depth approximately the same as that of the basic state current ($z_s = 115$ m). The short-scale vertical variations in the baroclinic instability mode's buoyancy field (Figure 4c) are correlated with similar variations in the basic state buoyancy field obtained from measurements taken in the California Current system, a region of active mixing between multiple water masses, near 41.5°N (Figure 2a) [Kosro et al., 1991]. The baroclinic instability mode's vertical velocity has a subsurface maximum centered on 100 m depth and $x = x_f$. In contrast, the frontal mode's signal is trapped more closely to the surface and to the frontal region ($x = x_f$). The short-wavelength mode's vertical e-folding scale ranges from 30–60 m depending on which field is examined. The frontal mode's cross-stream velocity tilts slightly with depth and the along-stream and buoyancy fields are asymmetric with respect to the surface front ($x_f = 30$ km), with the largest signals found on the inshore side of the front. The short-wavelength mode's buoyancy field has a secondary maximum at 65–70 m which correlates with the region of maximum stratification in the basic state density profile (Figure 2a).

The frontal mode's vertical velocity has a subsurface maximum at a depth of 30 m, just above the main thermocline, which begins at approximately 50 m, and has

slightly higher values offshore of $x = x_f$. Since vertical velocity is important to physical and biological processes in the upper ocean and is notoriously difficult to measure directly, it is useful to relate the magnitude of the subsurface vertical velocity maximum to the wave's relatively easily measured temperature anomaly (measurable, for example, by moored or drifting temperature recorders or by satellite imagery). The ratio of the maximum buoyancy perturbation (at $z = 0$ m) to the maximum vertical velocity (at $z = 30$ m) is 3.6. To substitute temperature for buoyancy, this ratio should be divided by g (9.8 m s^{-2}) and the coefficient of thermal expansion ($\alpha = 2 \times 10^{-4}$ °C^{-1}). The final result is $|T'|_{max}/|w'|_{max} = 1838$. Using the maximum SST anomalies from the frontal waves in Figure 1 ($|T'|_{max} = 0.35$°C), a vertical velocity of 2×10^{-4} m s^{-1} (20 m d^{-1}) should result. In contrast, a similar calculation for the baroclinic instability mode yields a maximum vertical velocity at 100 m of 1.4×10^{-5} m s^{-1} (1.4 m d^{-1}), an order of magnitude smaller than for the frontal mode. This small vertical velocity is also consistent with the baroclinic instability mode being primarily quasi-geostrophic.

Vertical and horizontal phase shifts in perturbation cross-stream velocity, along-stream velocity, and buoyancy are useful in determining the major energy transfer mechanisms and the direction in which they transfer energy between the basic state flow and the growing perturbations. Conclusions based on examining these phase shifts, briefly summarized here, are confirmed by calculating directly the energy transfer terms ((12c)–(12h) but without the area integral) as presented below. As was true for the perturbation fields themselves (Figure 4), significant vertical phase shifts for the frontal mode occur in the upper 60 m or less, while those for the baroclinic instability mode extend deeper into the water column. Vertical phase changes in cross-stream velocity and buoyancy for both modes are consistent with extraction of basic state energy via baroclinic instability. Vertical phase shifts in along-stream and vertical velocity for both modes are consistent with extraction of energy from the basic state via vertical Reynolds stress. Horizontal phase changes in cross-stream velocity for the baroclinic instability mode indicate unidirectional extraction of basic state kinetic energy via barotropic instability, while for the frontal mode there exist regions of significant transfer of perturbation energy back to the basic state via horizontal Reynolds stress. These interpretations of energy transfer are confirmed below and in section 5 where results from a time-dependent numerical model are discussed.

Each of the energy transfer terms ((12c)–(12h) without the area integral) for the two fastest-growing modes is shown in Figure 5. The horizontal heat flux (HHF) is positive everywhere (energy flowing from the basic state to the perturbations via baroclinic instability) for both modes. For the baroclinic instability mode the horizontal Reynolds stress (HRS) is positive everywhere, while for the frontal mode HRS shows a significant region where the perturbations are feeding the basic state
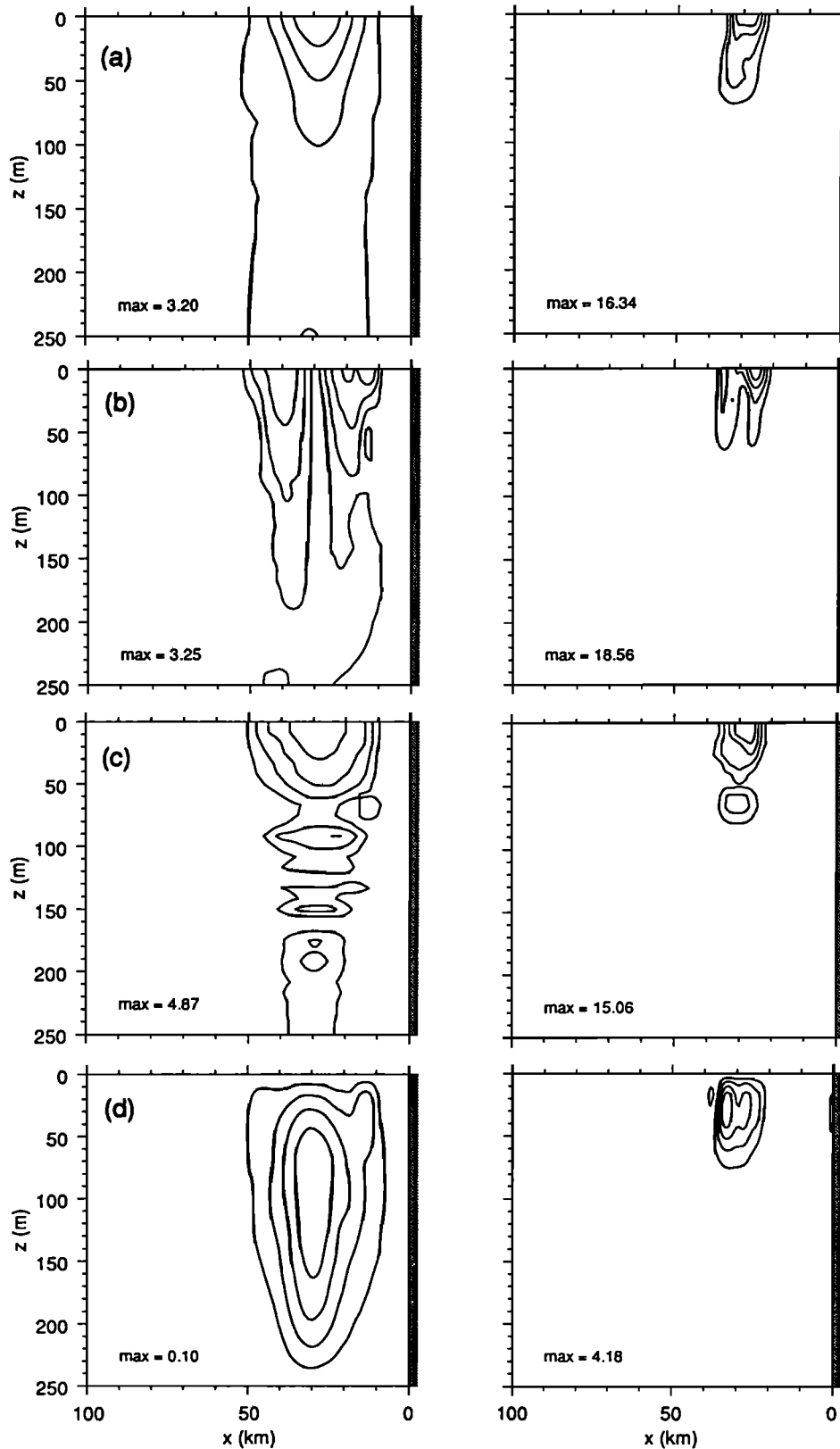
Figure 4. Structure of the fastest-growing (left panels) baroclinic and (right panels) frontal instabilities: (a) cross-stream velocity; (b) along-stream velocity; (c) buoyancy; (d) vertical velocity. Contours are 0.2 to 1 by 0.2 where each field has been normalized by its maximum value as noted in each frame. Although the plots extend to 100 km offshore, the stability calculation is restricted to $x \leq L = 75$ km.
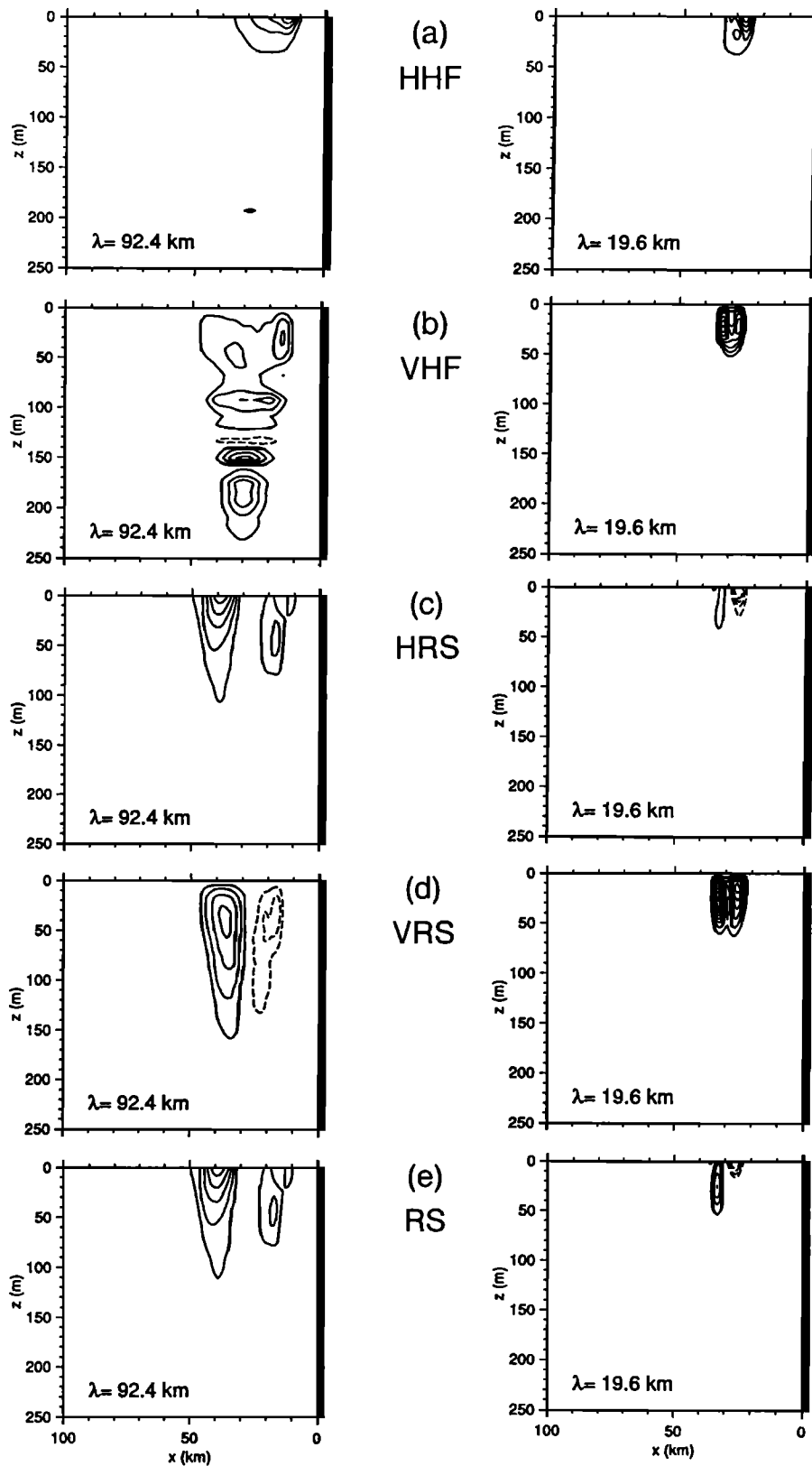
Figure 5. Structure of the energy transfer terms defined by (12) but without the area integral for the fastest-growing baroclinic (left panels) and frontal (right panels) instabilities. RS is the sum of HRS and VRS. Contours (min, max, inc), where the zero contour is never plotted for the baroclinic instability are on the left (a) HHF (0.5, 2.5, .5), (b) VHF (-0.02, 0.08, 0.02), (c) HRS (0.05, 0.25, 0.05), (d) VRS (-0.004, 0.008, 0.002), (e) RS (0.05, 0.25, 0.05). Contours for the frontal instability are on the right (a) HHF (10, 60, 10), (b) VHF (2, 14, 2), (c) HRS (-8, 2, 2), (d) VRS (0.5, 4.5, 0.5), (e) RS (-8, 8, 2).

(a) baroclinic instability mode (λ=92.4 km)

(b) frontal instability mode (λ=19.6 km)
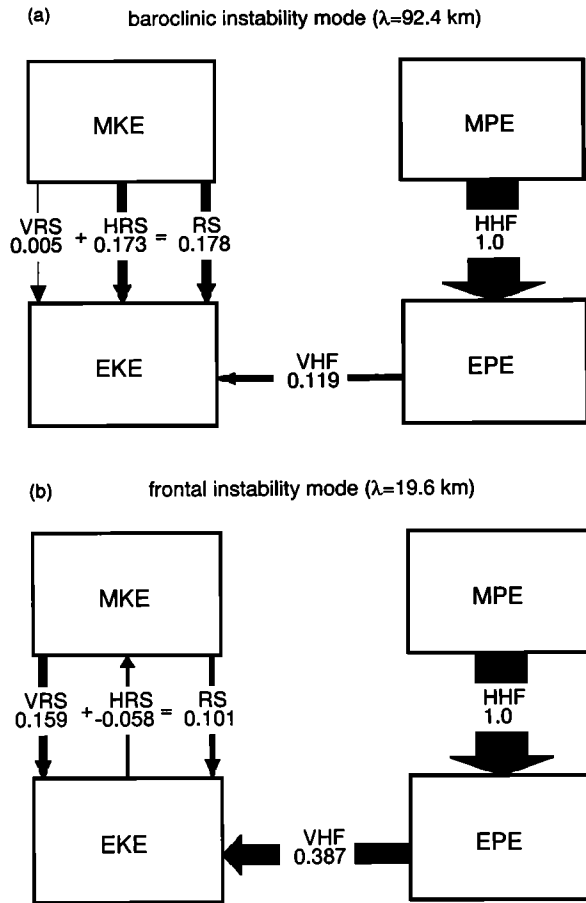
Figure 6. Block energy diagrams for the fastest-growing (a) baroclinic and (b) frontal instabilities. The arrow widths are proportional to the size of the indicated energy transfer which have been normalized by the value for HHF.

(HRS < 0). The vertical Reynolds stresses (VRS) are predominately positive for both modes, with a small region of energy transfer from the perturbations to the basic state (VRS < 0) onshore of $x = x_f$ for the baroclinic instability mode. Finally, note that the total Reynolds stress (RS) is dominated by HRS for the baroclinic instability mode while both HRS and VRS contribute significantly to RS for the frontal mode.

A summary of the energy transfers for each mode is given by a box energy diagram (Figure 6) where each value represents an area average normalized by the value for HHF. Energy in the basic state is designated as mean kinetic energy (MKE) and mean potential energy (MPE). Again, both modes grow primarily from baroclinic instability with an additional 18% coming via RS in the longwave mode and 10% for the frontal mode. The baroclinic instability mode's RS contribution is primarily from a barotropic instability mechanism (HRS). In contrast, the frontal mode is transferring energy to the basic state flow via HRS (the opposite to traditional, short-wavelength Rayleigh shear instability) while gaining energy via VRS in a Kelvin-Helmholtz-type mechanism.

To understand further the relationship of the frontal instability model to the basic state characteristics and in anticipation of contrasting the structure of the frontal mode with that of a fundamentally different inertial instability described in section 4.4, fields of the basic state Richardson number

$$Ri = \frac{N^2}{V_z^2} = \frac{f^2 B_z}{B_x^2} \tag{14}$$

and the potential vorticity
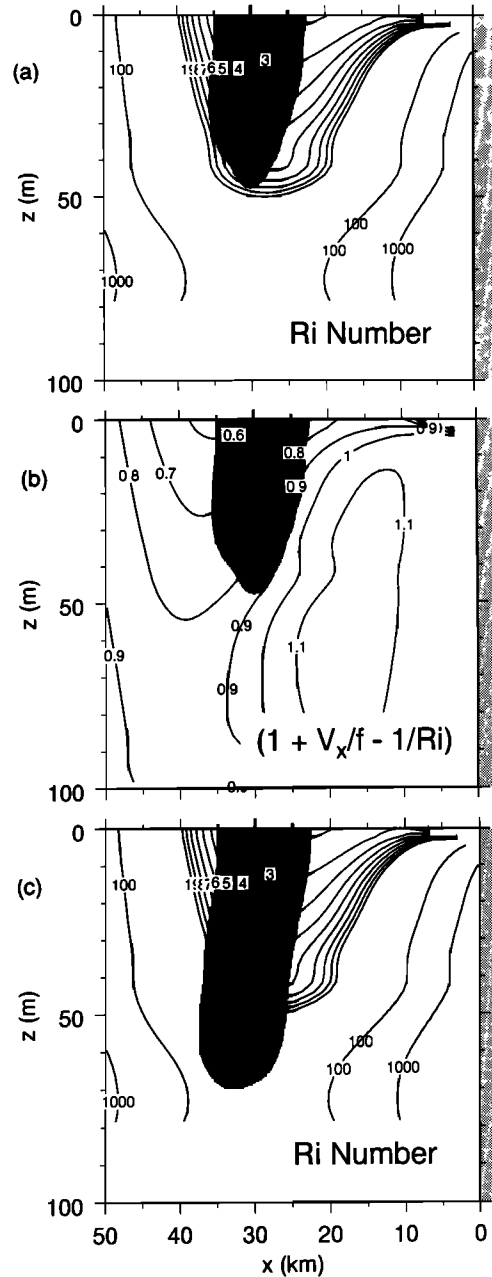
Figure 7. Figures 7a and 7c are contours of Ri and Figure 7b is $(1 + V_x/f - 1/Ri)$ near the surface front. Shading indicates regions of significant HHF (Figures 7a and 7b) or where the magnitude of the perturbation cross-stream velocity exceeds 0.2 of its maximum value (Figure 7c) for the frontal instability mode.

$$Q = \frac{\rho_0 f N^2}{\rho g}\left(1 + \frac{V_x}{f} - \frac{1}{Ri}\right) \qquad (15)$$

are plotted for the region near the front in Figure 7. In regions of strong horizontal and vertical current shear, the potential vorticity field differs from that typically used to describe large-scale oceanic circulation $[Q = (f/\rho)\partial\rho/\partial z)]$ by the factor in the parenthesis of (15). Further, the sign of the term in parenthesis is relevant for assessing the possibility for inertial instability [Hoskins, 1974], therefore this term is plotted in Figure 7. Since the basic state flow is symmetric with respect to x_f, horizontal asymmetries in Ri and Q result from asymmetry in N^2. Nowhere is Q negative, so this flow does not satisfy the condition for inertial instability. Contours of the frontal mode's main energy source term (HHF) are drawn on top of Ri and Q. Note that the HHF structure lines up more closely with the region of low Ri than it does with the region of low Q. The frontal mode's cross-stream velocity structure correlates with that of HHF and with the region of low Ri. In summary, the short-wavelength frontal mode is a result primarily of baroclinic instability, with a significant contribution from a Kelvin-Helmholtz-type mechanism. It is not a traditional, short-wavelength Rayleigh horizontal shear instability because the energy transfer via HRS is from the perturbations to the basic state. Finally, this mode is not an inertial instability where significant perturbation amplitudes and energy transfers would align with regions where $Q < 0$ (see section 4 for an example).

4. Parameter Variation Experiments

A number of studies were carried out to examine the dependence of the unstable waves characteristics on both the properties of the basic state flow (strength of the vertical and horizontal shear) and on the inclusion of horizontal friction and linearly sloping bottom topography. The focus here will be on the behavior of the frontal instability since the effects on the traditional baroclinic instability mode have been studied previously [see Barth, 1989b, and references therein].

4.1. Effects Due to Varying Vertical Shear

To examine the influence of the strength of the basic state vertical shear, an analysis was carried out with $z_s = 100$ m, that is, for an increased vertical shear. The results for the frontal instability are shown for $z_s = 100$ m (dashed curves) together with those using the basic state ($z_s = 115$ m, solid curves) in Figure 8. The growth rate of the fastest-growing mode increases with increased basic state vertical shear (e-folding now in 1.06 days), but its wavelength is only slightly reduced ($\lambda = 18.7$ km). Similarly, the magnitude of the phase speed is slightly reduced over all wavenumbers. The frontal instability's growth rate increases with increasing basic state vertical shear consistent with its growth via a baroclinic instability process. The growth rate is rather sensitive to changes in basic state vertical shear
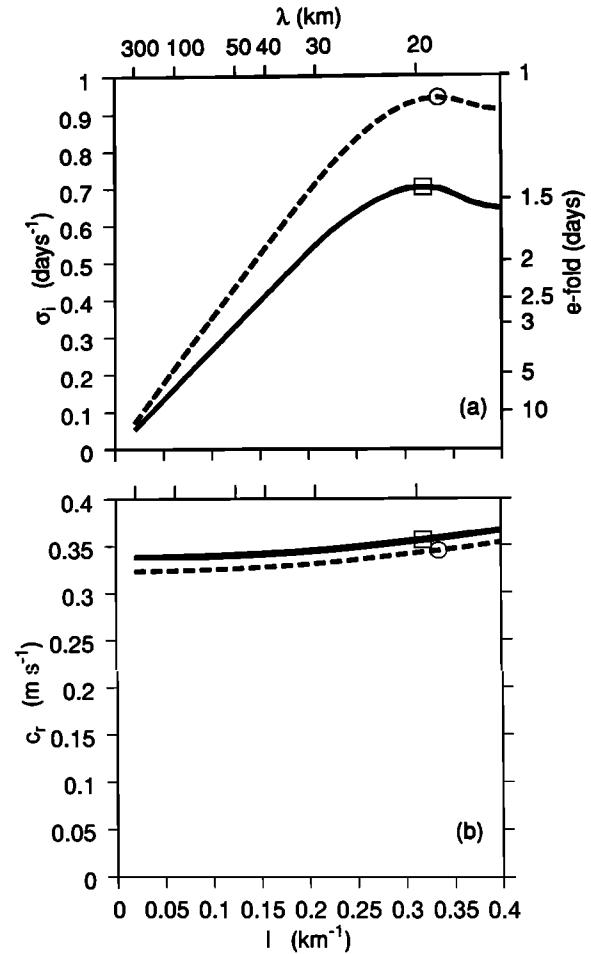
Figure 8. (a) Growth rates and (b) phase speeds for the frontal instability with $z_s = 100$ m (dashed curves) and $z_s = 115$ m (solid curves).

as evidenced by a 35% increase in σ_i for a 15% increase in vertical shear.

4.2. Effects Due to Viscosity

Viscous processes, whether internal to the fluid or via bottom friction or both, are known to affect the properties of growing unstable waves. To explicitly include these effects, drag terms (e.g., Laplacian or biharmonic damping) could be added to the right-hand sides of (1) and then the linear stability analysis could be repeated [e.g., Barth, 1989b]. In fact, this is the only way to properly include friction when the possibility exists that it may destabilize the system [Holopainen, 1961; Barth, 1989b]. Alternatively, an estimate of the effect of friction on the unstable waves can be made by comparing the e-folding timescale for the waves to the decay timescale due to friction. With an eye toward commenting on the level of dissipation employed in recent three-dimensional, time-dependent numerical models of unstable jets and fronts, dissipation is included as biharmonic damping. The relevant inverse decay timescale for motion at a wavelength λ is then $\sigma_4(s^{-1}) = 4\nu_4\left(\frac{2\pi}{\lambda}\right)^4$, where ν_4 (m^4 s^{-1}) is the biharmonic friction coefficient. For different values of ν_4 this

inverse decay timescale was subtracted from the inviscid growth rate curves for both the traditional baroclinic instability (Figure 9a) and the frontal instability (Figure 9b). The fastest-growing baroclinic instability mode is basically unaffected by biharmonic dissipation up to at least $\nu_4 = 1 \times 10^9$ m^4 s^{-1}. For weak dissipation ($\nu_4 = 1 \times 10^7$ m^4 s^{-1}) the fastest-growing frontal mode is slightly damped and has its wavelength shifted to a slightly longer value. However, for $\nu_4 = 1 \times 10^9$ m^4 s^{-1}, the frontal mode is severely damped. Recent numerical models [*Haidvogel et al.*, 1991a; *McCreary et al.*, 1991] have used biharmonic friction coefficients in the range 2.5–5 × 10^9 m^4 s^{-1}, effectively limiting their ability to study these short-wavelength instabilities, as noted by *McCreary et al.* [1991]. In section 5 the linear stability predictions for the inviscid frontal instability are compared to the early stages of a three-dimensional, time-dependent numerical model where there is sufficient horizontal resolution to keep the dissipation weak ($\nu_4 = 1 \times 10^7$ m^4 s^{-1}).

4.3. Effects Due to Bottom Topography

Because coastal upwelling often occurs over a sloping continental shelf and slope, the influence of linearly sloping bottom topography on the unstable modes is
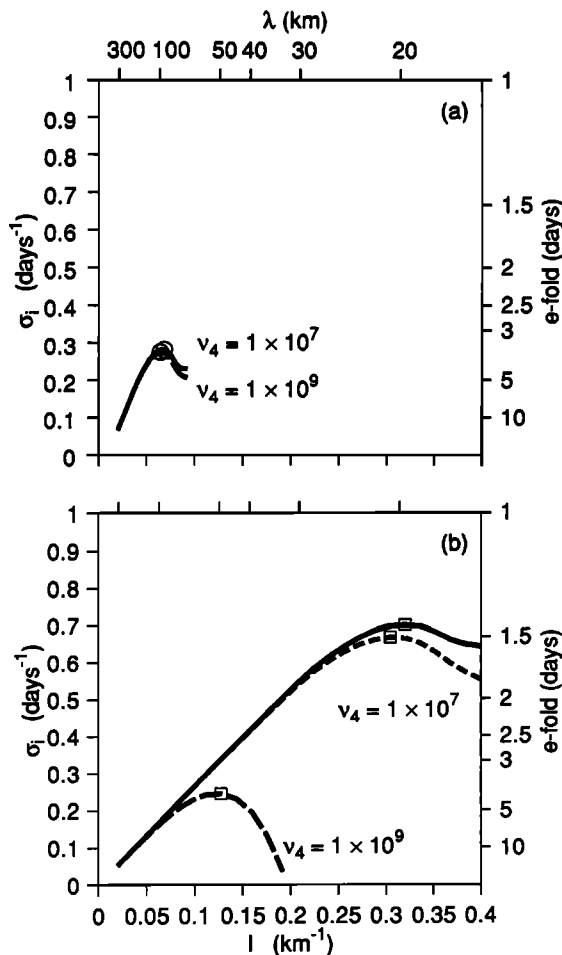

Figure 9. Growth rates minus the decay times for several values of the biharmonic friction coefficient for the (a) baroclinic and (b) frontal instabilities.
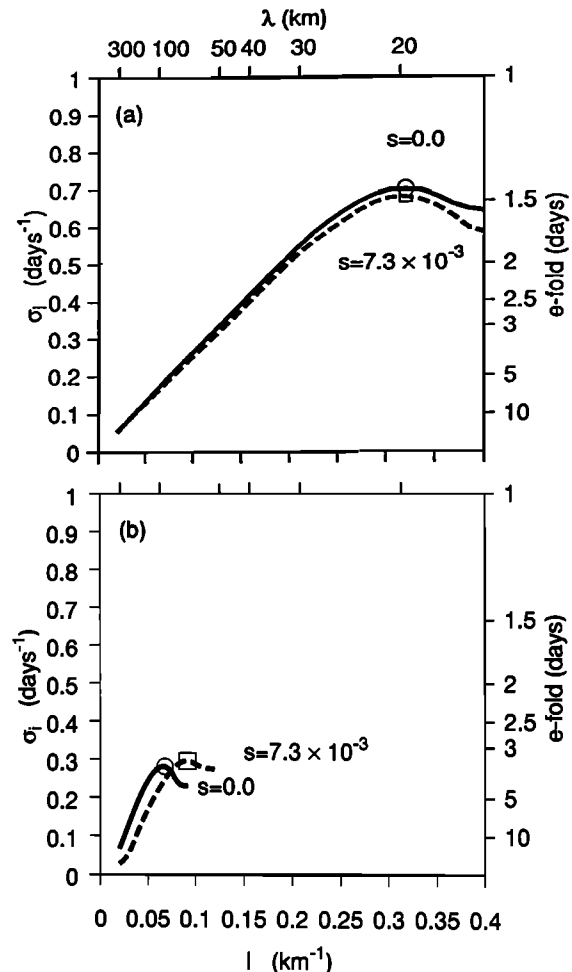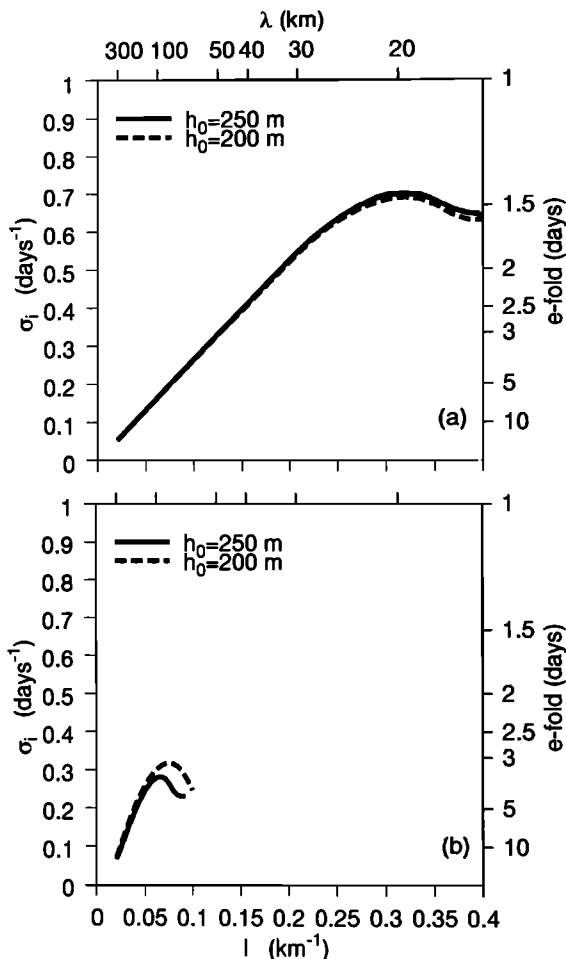

Figure 10. Growth rates for a flat bottom model (solid curves) and for a linearly sloping bottom (dashed curves) for the (a) frontal and (b) baroclinic instabilities.

investigated. In the work by *Barth* [1989b], a sloping bottom reduced the growth rates of the traditional baroclinic instability mode in a two-layer coastal upwelling jet, and for a large enough bottom slope the system could be completely stabilized. The present model differs by (1) including stratification in the lower part of the water column beneath the coastal jet which may insulate it from the effects of topography and (2) including dynamics capable of supporting the frontal instability. (The geostrophic momentum approximation employed by *Barth* [1989a,b] filters out the frontal instability [*Moore and Peltier*, 1989].) The bottom depth at $x = x_f$ is kept the same as in the flat bottom case ($h_0 = 250$ m) but then is decreased linearly to 30 m at the coastal wall ($x = 0$) so that the bottom slope is 7.3 × 10^{-3}, a typical value for the continental shelf off the U.S. west coast. In Figure 10 the growth rates for the sloping bottom case (dashed curves) are compared to those for a flat bottom (solid curves) for the two unstable modes. The frontal mode is essentially unchanged, with only a slight decrease in maximum growth rate but no change in phase speed (not shown), reflecting the fact that this mode is concentrated in the

Figure 11. Growth rates for the flat bottom (a) frontal and (b) baroclinic instability modes for two values of the bottom depth.

upper 70 m of the water column. The traditional baroclinic instability mode is stabilized by topography at low wavenumbers as expected, but the fastest-growing wave has a slightly greater growth rate and is shifted to a higher wavenumber. This is because the region of significant horizontal heat flux for this mode is concentrated inshore of $x = x_f$ (Figure 6a, left panel) where the destabilizing influence of shallow water comes into play [*Barth*, 1989b].

To verify the effect of shallow water on the unstable modes, the basic case, flat bottom calculation is repeated but now using $h_0 = 200$ m. The growth rate of the frontal instability (Figure 11a) is virtually unaffected by changes in h_0, again because it is a surface-concentrated phenomenon. In contrast, the growth rate for the baroclinic instability in the shallow case (dashed curve in Figure 11b) is greater at all wavenumbers than for the basic case and the fastest-growing wave occurs at a shorter wavelength. The shift to higher wavenumber occurs because the fastest-growing wave's Rossby height, $H_R = f/(Nl_{max})$, must decrease as h_0 decreases in order to maintain the optimum ratio for growth via baroclinic instability (see *Gill* [1982, section 13.3] in terms of Eady's model). The larger growth rate results

because the higher-wavenumber fastest-growing wave again has a shorter Rossby height so that the mode essentially sees the increased vertical shear closer to the sea surface, (13). The maximum growth rate is 13% greater than for the $h_0 = 250$ m case, less than the 21% increase predicted by *Killworth et al.* [1984], who found a strong dependence of growth rate on lower-layer depth in their two-layer, primitive equation model. Evidently, the reduced sensitivity of growth rate to changes in h_0 found here is a result of the presence of stratification in the lower water column. The 9% reduction in the fastest-growing wavelength for $h_0 = 200$ m compared with that for $h_0 = 250$ m is in excellent agreement with the predicted changes from *Killworth et al.* [1984], who found λ_{max} proportional to $h_0^{1/4}$.

In summary, the influence of bottom topography on the frontal instability is expected to be minimal, while its effect on the traditional baroclinic instability mode will depend on the relationship between the jet/front and the continental shelf and slope topography. For example, the susceptibility of the coastal upwelling jet/front off the U.S. west coast to traditional baroclinic instability may change as the jet, which forms over the shallow continental shelf, transits the continental slope to contribute to (or, in fact, become) the meandering jet found in typical eastern boundary current regions. This hypothesis deserves future attention.

4.4. Effects Due to Varying Horizontal Shear

The dependence of both the frontal instability and the traditional baroclinic instability on the magnitude of the jet's horizontal shear is investigated. This will help relate both modes to the known behavior of classic baroclinic and barotropic (Raleigh shear) instability as well as help to shed light on the possibility for inertial instability when x_d is small enough so that the horizontal shear is comparable to the Coriolis parameter. In Figure 12 the growth rates for the two modes are shown for three values of x_d. The maximum growth rate for the baroclinic instability mode increases as x_d decreases, consistent with the fact that this mode has a contribution to its growth via horizontal Reynolds stress (Figure 12a). For the basic case ($x_d = 15$ km) the HRS conversion is 17% of the HHF contribution (Figure 6a), while for $x_d = 20(10)$ km it is 4% (114%). For the long-wavelength mode on a narrow front ($x_d = 10$ km), growth via HRS is as important as growth via HHF and this mode's vertical structure extends deeper into the water column compared with the wide-front modal structures, consistent with a significant contribution via a barotropic energy conversion mechanism (HRS). Finally, the magnitude of c_r decreases as x_d decreases for the baroclinic instability mode (not shown).

In contrast, the maximum growth rate of the frontal mode decreases significantly as x_d decreases (Figure 12b). For $x_d = 20$, 15, and 10 km the e-folding time for the fastest-growing mode is 1.10, 1.43, and 1.73 days, respectively, so that a 50% decrease in x_d results in a roughly equivalent increase in the e-folding time. The wavelength of the fastest-growing wave increases
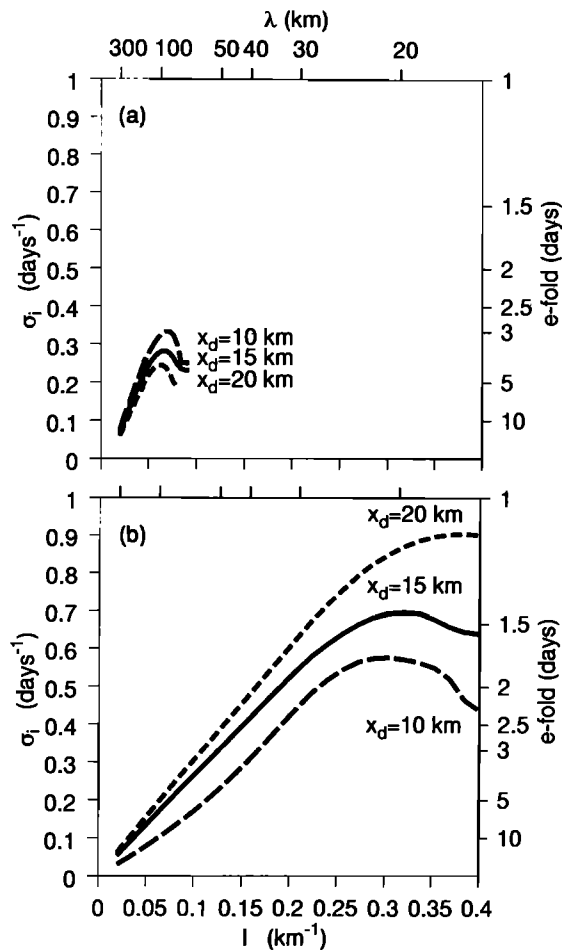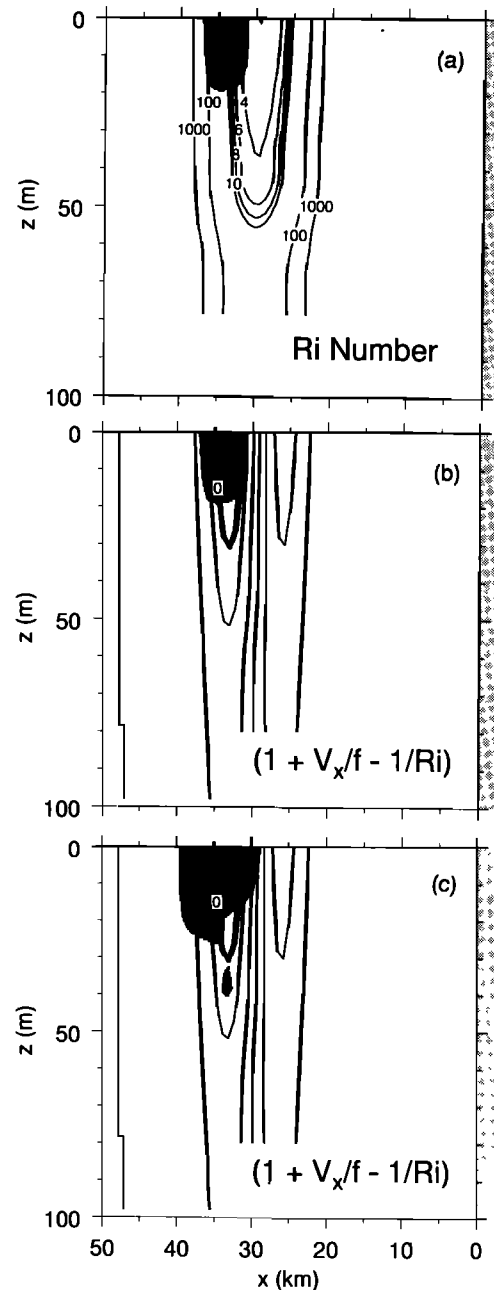
Figure 12. Growth rates for three values of the jet's Gaussian half-width for the (a) baroclinic and (b) frontal instabilities.

make $R_i < 1$, then $Q < 0$ from (15) and so-called symmetric instability will result [Stone, 1966]. The fastest-growing perturbation in this case will have no structure in the direction of the basic state flow. That is, the disturbance will not be wavelike along the jet or alternatively $\ell = 0$. However, when horizontal shear is also present the fastest-growing mode will have a nonzero along-stream wavenumber and should be called inertial instability [Stevens and Ciesielski, 1986].

slightly ($\lambda_{max} = 16.4$, 19.6, 20.7 km) as x_d decreases ($x_d = 20$, 15, 10 km) and, as for the baroclinic instability mode, the phase speed lessens as the frontal zone narrows. To understand the frontal mode's behavior, consider the ratio of the natural length scale in the system, the internal Rossby radius of deformation, R, to the half-width of the jet, x_d. As x_d decreases relative to R, the jet/front becomes too narrow for the frontal instability to extract its main source of energy via baroclinic instability. Further, the conversion by HRS is small for all x_d, being negative for $x_d = 20$, 15 km (HRS = -3%, -6%) and only slightly positive for $x_d = 10$ km (HRS = 3%), where again HRS is scaled by the magnitude of the HHF conversion term. That $\sigma_{i_{max}}$ decreases as the horizontal shear increases is further proof that this mode is not like a Raleigh shear instability where $\sigma_{i_{max}}$ is proportional to the magnitude of the horizontal shear.

When the jet half-width (x_d) is small enough so that the magnitude of the horizontal shear is comparable to f, regions with $Q < 0$ can occur on the anticyclonic side of the jet. This allows for the possibility for inertial instability [Hoskins, 1974]. When horizontal shear is absent and the vertical current shear is strong enough to

Figure 13. As in Figure 7, but for the inertial instability mode. Shading in Figure 13a and Figure 13b indicates regions of significant energy transfer by HRS while in Figure 13c it highlights the region where the magnitude of the perturbation cross-stream velocity exceeds 0.2 of its maximum value. Contours for $(1+v_x/f-1/Ri)$ are -0.2 (dashed line), 0.0 (thick line) and 0.2 to 1.8 by 0.4 (solid lines).

inertial instability mode
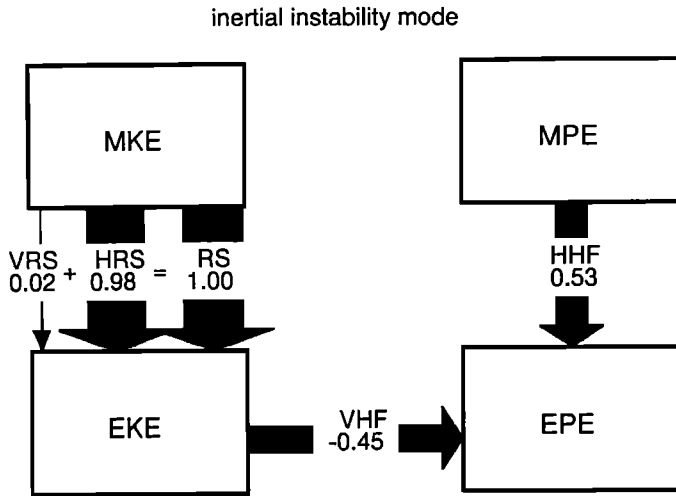
Figure 14. As in Figure 6, but for the inertial instability with $\ell = 0.02$ and energy transfer terms are normalized by the value for the total Reynolds stress (RS).

For the jet described by (14) with $v_0 = 0.7$ m s^{-1} and $x_d = 5$ km, a region with $Q < 0$ is found offshore of $x = x_f$ (Figure 13b). For $\ell = 0.02$ the stability analysis yields a new fastest-growing mode with $\sigma_i = 0.345$ day^{-1} where the previously described frontal and traditional baroclinic instability modes have $\sigma_i \leq 0.125$ day^{-1}. This inertial instability mode is growing primarily by conversion of MKE to EKE via HRS (Figure 14). The region of active energy conversion by HRS is essentially confined to the region where $Q < 0$ as expected for an inertial instability (Figure 13b). The cross-stream velocity (Figure 13c) and HRS correlate very closely with each other and with the region of $Q < 0$ but not with the region of low Ri (Figure 13a). In summary, this mode is only present when there exists a region in the flow with $Q < 0$ and its energetics and velocity structure are distinct from the previously described frontal instability mode. Whether or not regions with $Q < 0$ exist in coastal upwelling jets and fronts found in nature is a matter for investigation, but evidence suggests that local Rossby numbers can be quite high [*Paduan and Niiler*, 1990].

5. Comparison With Nonlinear, Time-Dependent Numerical Model Results

To verify the linear predictions described in the previous sections and to set the stage for further nonlinear, finite-amplitude studies, the stability of a coastal upwelling front and jet is examined using a time-dependent numerical model. The model is a periodic channel version of a semispectral, primitive equation ocean circulation model using bottom-following (sigma) coordinates in the vertical and orthogonal curvilinear coordinates in the horizontal [*Haidvogel et al.*, 1991b]. To allow sufficient room for the long-wavelength instability to

grow, the periodic channel is 200 km long. The offshore edge of the domain is placed far enough away (150 km) so that the channel wall placed there does not affect the dynamics near the surface front at 30 km offshore.
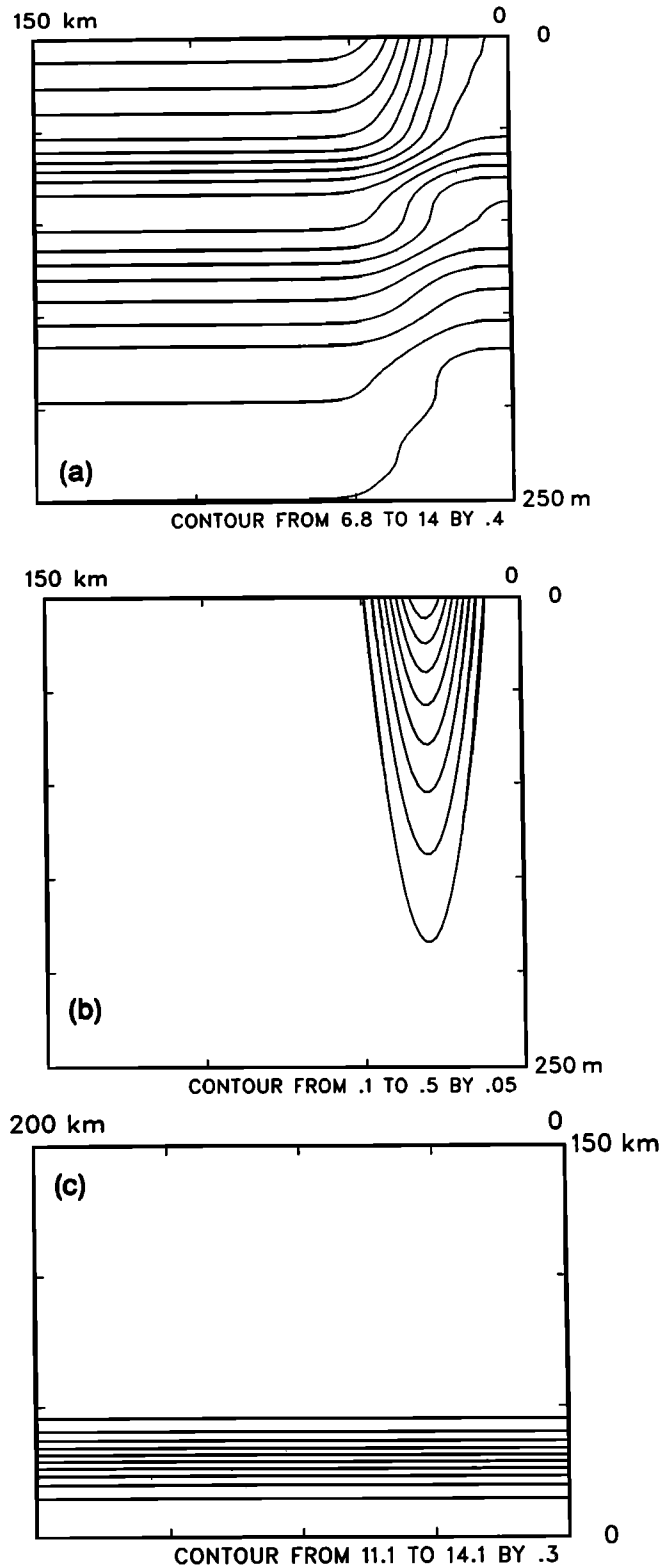

Figure 15. Vertical sections of (a) temperature (°C), (b) along-channel velocity (m s^{-1}) and (c) a plan view of surface temperature (°C) used as initial conditions for the numerical model.

The model grid is uniform in the along-channel direction (136 points, $\Delta y = 1.5$ km) and is stretched in the across-channel direction to provide the greatest resolution near the front (76 points, 1.5 km $< \Delta x <$ 2.5 km). The model is spectral in the vertical, and 21 Chebyshev polynomials are used over 250 m where the minimum grid spacing is 2 m and the maximum is 20 m. With these choices, the model is run stably with a time step of 5 minutes. On a Cray Y-MP, one day of simulation takes approximately 6 CPU minutes. Finally, biharmonic horizontal friction is included with $\nu_4 = 1 \times 10^7$ m^4 s^{-1} so that the decay timescale for a 20-km feature is 30 days. This level of biharmonic friction is 2 orders of magnitude less than that used in other recent eastern boundary current models [McCreary et al., 1991; Haidvogel et al., 1991a]. A small amount of Laplacian vertical friction is also included at a level ($\kappa = 2 \times 10^{-4}$ m^2 s^{-1}) that results in a damping timescale, for features with the vertical scale of the frontal instabilities, that is significantly longer than the decay timescale due to horizontal mixing.

The initial velocity and temperature fields (salinity is passive in these model runs) are the same as in the basic case linear stability analysis (section 3). That is, the along-channel velocity is given by (13) with $v_0 = 0.5$ m s^{-1}, $z_s = 115$ m, $x_f = 30$ km, $x_d = 15$ km (Figure 15b), and the temperature field is found by integrating the thermal wind equation at each z level from far offshore, through the frontal zone, to the coast (Figure 15a). In plan view the upwelling jet is flowing from right to left along the coast-parallel temperature contours (Figure 15c). To allow the instabilities to manifest themselves sooner, a perturbation, in thermal wind balance made up of 10 along-channel wavenumbers with random phase and whose summed amplitude is 10% of the basic state along-channel flow, is added to the initial basic state velocity and temperature fields. The noise field at $t = 0$ is specified to have the same cross-channel and depth dependence as the basic state flow (13).

Soon after the model run is initiated, perturbations with short along-front scales appear and grow rapidly. At $t = 3$ days they are quite evident in the total surface temperature field, $T(x, y, z = 0)$ (Figure 16a). When the along-channel-averaged temperature field, $\overline{T}(x, z)$, is removed, alternating bands of warm and cold water are clearly seen in the surface perturbation temperature field, $T'(x, y, z = 0)$ (Figure 16b). The perturbations are frontally trapped, have an along-front wavelength of 24 km and e-fold in approximately 1.4 days. The larger cross-front scale of the temperature perturbations apparent in Figure 16b compared with the cross-front scale of the perturbation buoyancy field from the linear prediction (Figure 4c), results because the initial noise field is specified to have the same cross-channel dependence as the basic state flow (i.e., Gaussian with a half-width of 15 km). The horizontal phase shift of the temperature perturbations (Figure 16b) is in the same sense as would be expected from a passive scalar sheared out by the basic state flow. This agrees with the linear prediction of energy transfer via HRS from


CONTOUR FROM 11.1 TO 14.1 BY .3

CONTOUR FROM -.2 TO .2 BY .04
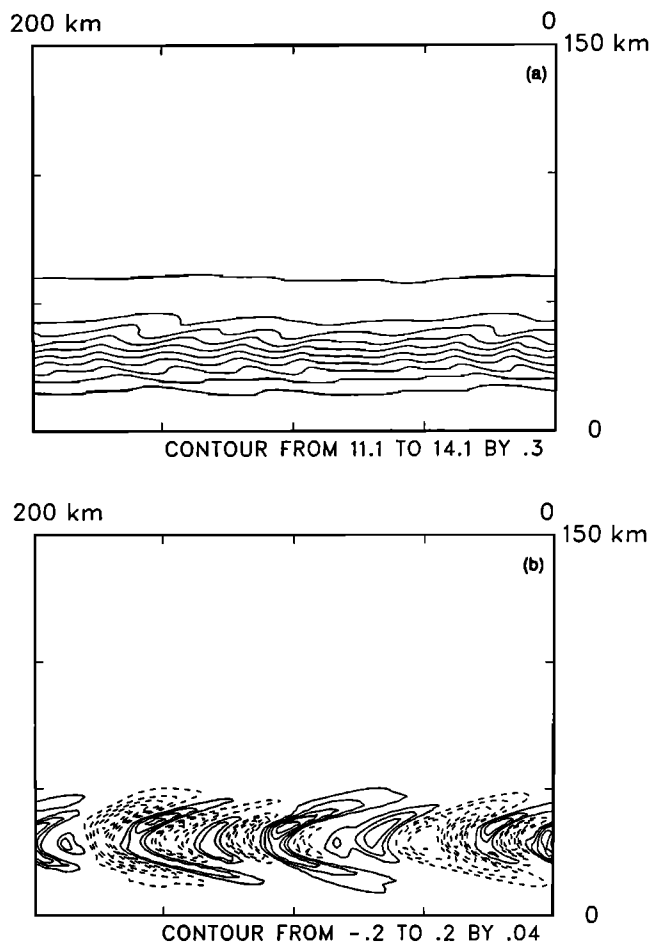
Figure 16. (a) Total temperature ($^\circ$C) and (b) temperature anomalies ($^\circ$C) at the surface at $t = 3$ days.

the perturbations to the mean; this is not a traditional, short-wavelength horizontal shear instability. In the SST perturbation field from off central Oregon (Figure 1b), there is a hint of the same sense of horizontal phase shift as seen in the model T' field (Figure 16b). As the model flow evolves, the temperature perturbations propagate in the same direction as the basic state flow, as evident in successive vertical sections of total temperature along the channel at the surface front, $T(x_f, y, z)$ (Figure 17). Growth of the instability is evident as subsurface isotherms erupt to the surface. The temperature perturbations are clearly surface trapped and are propagating at roughly 0.34 m s^{-1}. These estimates for wavelength, growth rate, and phase speed are in excellent agreement with the linear predictions obtained with $\nu_4 = 1 \times 10^7$ m^4 s^{-1} ($\lambda = 20.7$ km, e-fold $= 1.50$ days, $c_r = 0.36$ m s^{-1}) for the basic case (section 3).

The vertical structure of the frontal instability is revealed in a vertical section of perturbation temperature along the surface front, $T'(x_f, y, z)$ (Figure 18a). The temperature anomalies are surface intensified and show a weaker subsurface maximum at 70 m. The T' vertical structure is in excellent agreement with the linear prediction for the vertical distribution of the
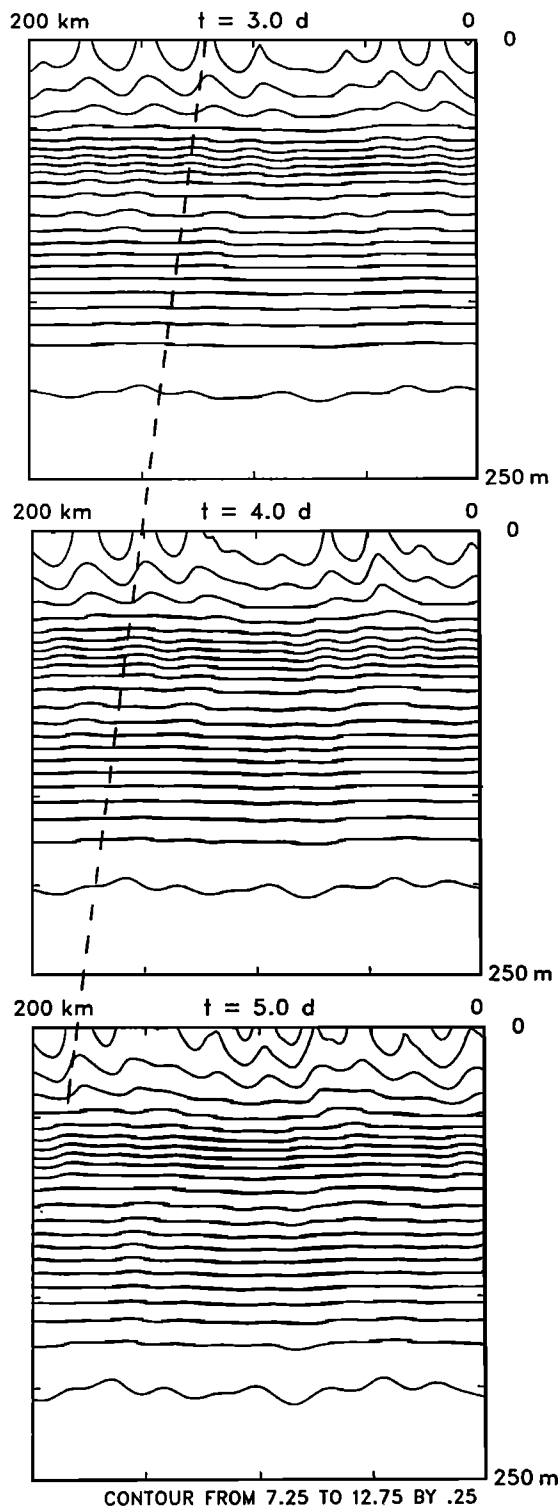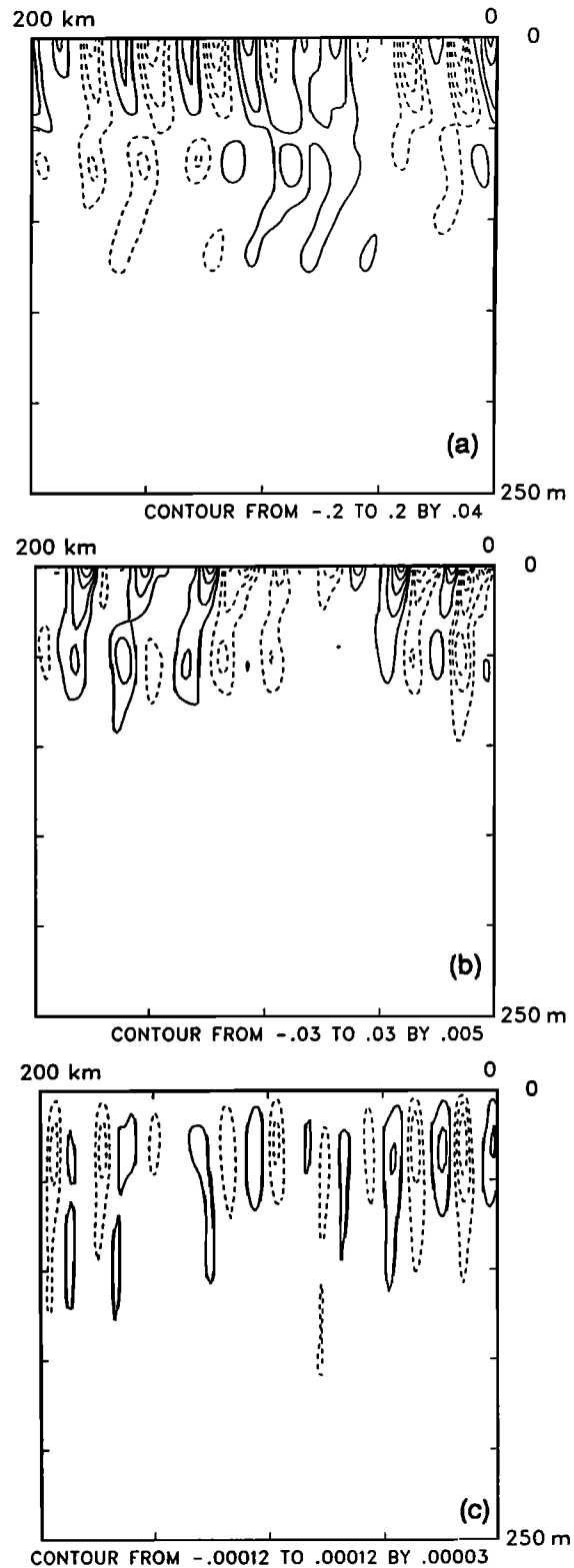
Figure 17. Vertical sections of total temperature (°C) along the channel at the surface front. The dashed line indicates phase propagation at 0.34 m s^{-1}.

fastest-growing frontal mode's perturbation buoyancy field (Figure 4c, right panel). The vertical phase shift is such that the perturbations are leaning in the same sense as the basic state vertical shear, confirming that the frontal mode is extracting energy from the mean flow by HHF. A vertical section of along-stream pertur-

bation velocity, $v'(x_f, y, z)$ (Figure 18b), again shows surface intensification, and the vertical phase shift leans against the basic state vertical shear consistent with the mode extracting mean kinetic energy via VRS. Finally,

Figure 18. Vertical sections of perturbation (a) temperature (°C), (b) along-channel velocity (m s^{-1}) and (c) vertical velocity (m s^{-1}) along the channel at the surface front at $t = 3$ days.
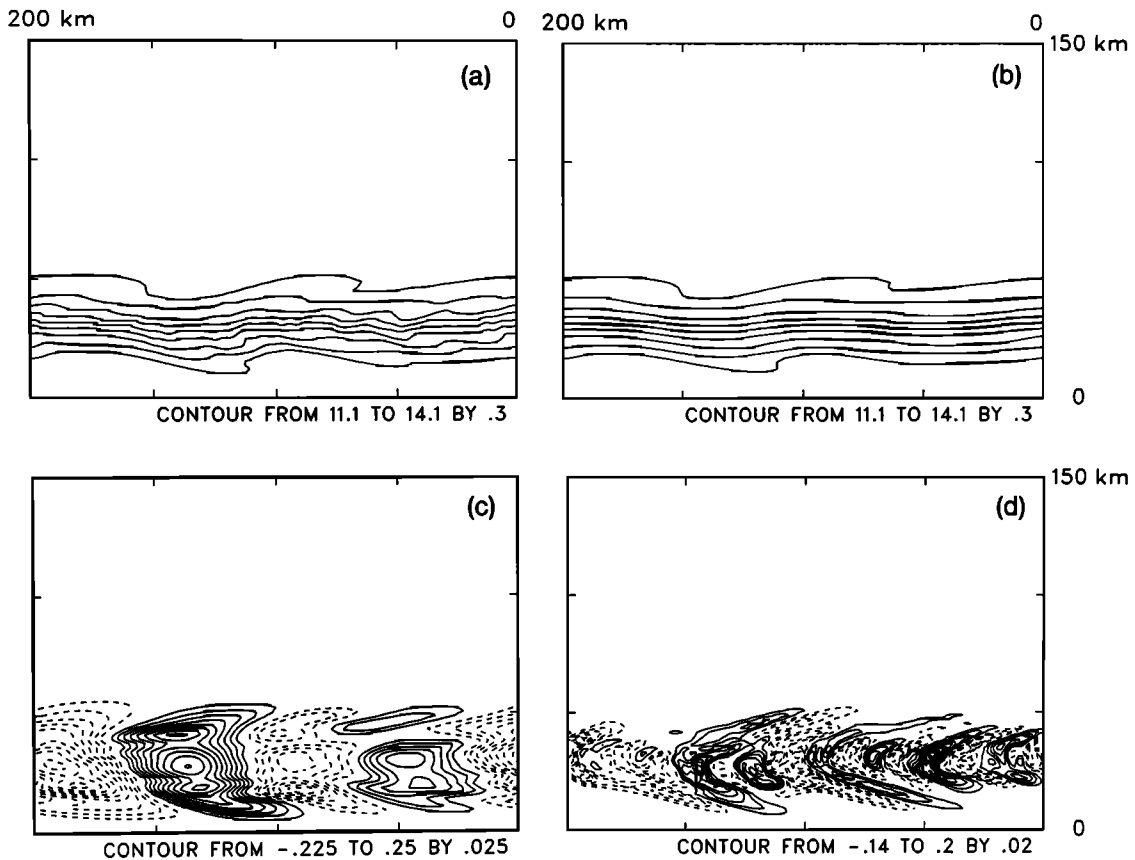
Figure 19. Temperature (°C) at the surface at $t = 9$ days: (a) Total, (b) cosine-filtered (filter widths: along-channel, cross-channel $= 45, 3$ km), (c) anomalies formed by subtracting the along-channel average, $\overline{T}(x, z)$, from the cosine-filtered field, (d) anomalies formed by subtracting the cosine-filtered field from the total temperature.

a similar vertical section of perturbation vertical velocity, $w'(x_f, y, z)$ (Figure 18c), shows a subsurface maximum at approximately 30 m in agreement with the linear prediction (Figure 4d, right panel). The ratio of the maximum temperature anomaly (Figure 18a) to the maximum vertical velocity anomaly (Figure 18c) is $|T'|_{max}/|w'|_{max} = 0.2°C/1 \times 10^{-4}$ m s$^{-1} = 2000$, in good agreement with the linear prediction (section 3).

The consistency between the results from the early stages of a nonlinear, time-dependent numerical model and the linear stability predictions verifies the existence of the frontal instability mode. A study of the behavior of the frontal mode at finite amplitude, including the interaction between it and the simultaneously growing long-wavelength, traditional baroclinic instability mode, is now possible. To show that the long-wavelength mode does eventually appear, the surface temperature field at $t = 9$ days is analyzed (Figure 19). A cosine-filtered version (Figure 19b) of the total temperature field (Figure 19a) exhibits a long-wavelength meander ($\lambda \simeq 104$ km), which is further highlighted when the along-channel-averaged temperature field, $\overline{T}(x, z)$ (not shown), is subtracted from the cosine-filtered field (Figure 19c). The long-wavelength mode e-folds in approximately 11 days and propagates at roughly 0.11 m s^{-1}. Superimposed on the long-

wavelength mode are the frontal instabilities which readily appear as short-wavelength temperature anomalies when the cosine-filtered temperature is subtracted from the total temperature field (Figure 19d). Notice that the train of short-wavelength anomalies tracks along the undulating path of the jet caused by the long-wavelength baroclinic instability mode; the anomalies do not line up in a straight line as at $t = 3$ days (Figure 16b). The estimates for the baroclinic instability mode's wavelength are in good agreement with the linear stability prediction from section 3 obtained with $\nu_4 = 1 \times 10^7$ m^4 s^{-1} ($\lambda = 98.2$ km, $c_r = 0.10$ m s^{-1}), but the growth rate is seriously underestimated (the linear prediction yields an e-folding period of 3.64 days). This may be a result of the presence of the frontal waves as they interact with the larger-scale instability and compete for the same energy supply from the mean flow. This nonlinear behavior is a subject for future investigation.

6. Discussion and Conclusions

The linear stability analysis presented here using the full primitive equations applied to a continuously stratified representation of a coastal jet and front successfully describes two modes of instability. A long-

wavelength mode is associated with traditional baroclinic instability and is a modified form of the mode that would result from a quasi-geostrophic analysis. A second, short-wavelength frontal instability is also found, which grows rapidly by extracting energy from the potential energy of the basic state flow. Linear predictions, obtained from the solution to an eigenvalue problem, for the frontal mode's fastest-growing wavelength, e-folding period, phase speed, and energetics are confirmed through the use of a fine-resolution, three-dimensional, time-dependent, nonlinear numerical ocean circulation model. A train of at least 10 regularly spaced short-wavelength temperature perturbations seen in a satellite SST image of a coastal upwelling front and jet off the U.S. west coast provides a typical example of these ubiquitous frontal instabilities. The frontal mode generates strong vertical velocities (20 m d^{-1} for 0.35°C surface temperature perturbations) in the upper part of the water column ($\lesssim 50$ m) which will affect the physical and biological fields in these regions. The frontal instability may also play a role in the ultimate dissipation of coastal jets and related offshore meandering jets, especially since observed turbulent dissipation rates associated with large-scale current shear have been low within these features [*Moum et al.*, 1988].

The properties of the frontal instability indicate that it is not a result of traditional horizontal shear instability nor is it an inertial instability which requires strong anticyclonic shears of the size of f. *Stone* [1966, 1970] demonstrated several aspects of the nongeostrophic baroclinic instability problem: (1) modification of the long-wavelength Eady mode by nongeostrophic effects for small enough Ri; (2) appearance of a symmetric mode of instability with large growth rate when $Ri < 1$; and (3) the presence of another mode of instability at short wavelengths with small growth rates. Although *Stone* [1966, 1970] did not analyze the third category of instability in detail, *Nakamura* [1988] studied it in a two-dimensional instability problem. He described the formation of the short-wavelength instability as a resonance between one boundary-trapped neutral Eady mode and an inertia-gravity mode leading to a baroclinic conversion of potential energy. *Nakamura's* [1988] short-wavelength modes were only weakly growing, which he attributed to the lack of three-dimensional structure in his model. A more detailed comparison between the rapidly growing, three-dimensional frontal instability found here and the short-wavelength mode found by *Stone* [1966, 1970] and described by *Nakamura* [1988] is an avenue for future research.

The short-wavelength instability discussed here can also be compared with other recent instability analyses which yield small-scale modes. *McCreary et al.* [1991] found a short-wavelength instability in a 2 1/2-layer model that allows a horizontal temperature gradient (a front) to develop in the uppermost mixed layer. Their short-wavelength instability grows by extracting the available potential energy associated with the horizontally variable upper layer temperature field. Although an inviscid linear stability analysis applied to

their basic state flow predicted the wavelength of the fastest-growing wave to be 8 km, they were unable to study the nonlinear evolution of the shortwave mode because the resolution of their numerical model was insufficient to allow stable runs with weak horizontal friction. Recently, Fukamachi et al. (submitted paper, 1994) have studied instabilities in a 1 1/2-layer model and a continuously stratified model. These models have horizontal temperature gradients in an upper layer whose depth is held constant. The continuously stratified model allows vertically sheared currents in the fixed-depth upper layer, which overlies a quiescent, stratified fluid. In contrast, the model presented here includes vertically sheared currents that extend throughout the water column. Fukamachi et al.'s (submitted paper, 1994) linear analysis of the 1 1/2-layer model confirms the findings of *McCreary et al.* [1991] and they find an analogous short-wavelength unstable mode in their continuously stratified model. They demonstrate that the high-wavenumber modes in their layered and continuously stratified systems are related, both being forms of ageostrophic baroclinic instability. In fact, Fukamachi et al.'s (submitted paper, 1994) short-wavelength instability is a nongeostrophic Eady mode [*Stone*, 1966, 1970] whose wavelength has been made small by confining the fluid to a shallow, fixed-depth upper layer. The perturbation density amplitude of their unstable mode has equally sized maxima at both the sea surface and at the bottom of the shallow upper layer, consistent with the Eady solution. This contrasts with the perturbation buoyancy amplitude of the short-wavelength mode found in this study which has a maximum at the sea surface and essentially decays away with depth (Figures 4 and 18). Another clear difference is that the fastest-growing, short-wavelength mode found by Fukamachi et al. (submitted paper, 1994) has a relatively slow phase speed of ~ 0.05 m s^{-1} while the short-wavelength mode described here has a fast phase speed of 0.36 m s^{-1}. Observations of short-wavelength meanders on coastal upwelling fronts can be used to determine which of these two types of short-wavelength modes is operative in nature. Such a study using satellite SST images to estimate phase speeds is underway, but a comparison of perturbation vertical structures will require less readily available in situ measurements.

A high-wavenumber mode found by *Barth* [1989b] in a two-layer model with a steeply sloping interface, equivalent to supercritical flow where the maximum of the basic state flow is greater than the internal gravity wave phase speed, was identified as growing primarily by conversion of basic state MKE to EKE and was related to the reduced gravity model results of *Killworth* [1983]. In fact, the high-wavenumber mode's growth rate is independent of the lower layer depth in the two-layer model confirming that it is a one-layer instability [*Barth*, 1987]. As pointed out by Fukamachi et al. (submitted paper, 1994), the steep interface slope condition is also equivalent to the potential vorticity field having a region with negative values, which satisfies the condition for inertial instability. In summary,

the high-wavenumber mode found by *Barth* [1989b] is likely to be most closely related to the inertial instability found in the continuously stratified flow considered in the present study (section 4.4). A comparison between these high-wavenumber modes in the two systems is planned for the future.

Recently, *Paldor and Ghil* [1991] have shown that a high-wavenumber mode whose growth rate increases linearly with wavenumber can exist in a two-layer model when either (1) the lower layer is significantly shallower than the active upper layer or (2) with fixed layer depths, the vertical shear exceeds some critical value. For fixed vertical velocity shear in their model, as the lower layer depth tends to infinity the instability exponent vanishes. Therefore the high-wavenumber, steep-interface mode found by *Barth* [1989b] is not the same mode as described by *Paldor and Ghil* [1991]. A comparison can also be made between the high-wavenumber mode found by *Paldor and Ghil* [1991] and the frontal mode described here. *Paldor and Ghil* [1991] do not completely describe the energetics of their high-wavenumber instability, but state that the conversion is both baroclinic and barotropic. They do not differentiate between VRS and HHF, but their emphasis on the similarity between their mode and traditional Kelvin-Helmholtz instability makes it likely that VRS is the dominant energy conversion process. This is not the case for the frontal mode found here (VRS is 11% of HHF, Figure 6) and, further, the frontal mode's growth rate curve turns down at high wavenumbers in contrast to the results of *Paldor and Ghil* [1991]. In summary, there appear to be distinct differences between the frontal mode described here and the high-wavenumber mode found by *Paldor and Ghil* [1991]. The continuously stratified model employed here will again allow a comparison of these modes, especially in terms of their energetics.

The good comparison between the early stages of the nonlinear, time-dependent numerical simulation and the linear stability predictions not only helps verify the existence of the frontal instability, but sets the stage for future finite-amplitude studies of the jet and front. In particular, the interaction between both modes of instability and the mean flow and between the two distinct bands of instability themselves is of interest. The numerical model also allows the inclusion of other physical processes important in the coastal ocean (e.g., wind forcing, alongshore topographic and/or bathymetric variations). Future studies will continue to elucidate the role of short-wavelength frontal instabilities in circulation over the continental margin.

References

Ahlnäs, K., T. C. Royer, and T. H. George, Multiple dipole eddies in the Alaska Coastal Current detected with Landsat thematic mapper data, *J. Geophys. Res.*, *92*, 13,041–13,047, 1987.

Allen, J. S., L. J. Walstad, and P. A. Newberger, Dynamics of the coastal transition zone jet, 2, Nonlinear finite amplitude behavior, *J. Geophys. Res.*, *96*, 14,995–15,016, 1991.

Arnone, R. A., and P. E. La Violette, Satellite definition of the bio-optical and thermal variation of the coastal eddies associated with the African Current, *J. Geophys. Res.*, *91*, 2351–2364, 1986.

Barth, J. A., Stability of a coastal upwelling front over topography, *Tech. Rep. 87-48*, 187 pp., Mass. Inst. of Technol. and Woods Hole Oceanogr. Inst., Woods Hole, Mass., 1987.

Barth, J. A., Stability of a coastal upwelling front, 1, Model development and a stability theorem, *J. Geophys. Res.*, *94*, 10,844–10,856, 1989a.

Barth, J. A., Stability of a coastal upwelling front, 2, Model results and comparison with observations, *J. Geophys. Res.*, *94*, 10,857–10,883, 1989b.

Gill, A. E., *Atmosphere-Ocean Dynamics*, 662 pp., Academic, San Diego, Calif., 1982.

Garvine, R. W., K.-C. Wong, G. G. Gawarkiewicz, R. K. McCarthy, R. W. Houghton, and F. Aikman III, The morphology of shelf break eddies, *J. Geophys. Res.*, *93*, 15,593–15,607, 1988.

Haidvogel, D. B., A. Beckman, and K. S. Hedström, Dynamical simulations of filament formation and evolution in the coastal transition zone, *J. Geophys. Res.*, *96*, 15,017–15,040, 1991a.

Haidvogel, D. B., J. L. Wilkin, and R. E. Young, A semispectral primitive equation ocean circulation model using vertical sigma and orthogonal curvilinear horizontal coordinates, *J. Comput. Phys.*, *94*, 151–185, 1991b.

Haynes, R., E. D. Barton, and I. Pilling, Development, persistence, and variability of upwelling filaments off the Atlantic coast of the Iberian Peninsula, *J. Geophys. Res.*, *98*, 22,681–22,692, 1993.

Holopainen, E. O., On the effect of friction in baroclinic waves, *Tellus*, *13*, 363–367, 1961.

Hoskins, B. J., The role of potential vorticity in symmetric stability and instability, *Quart. J. R. Met. Soc.*, *100*, 480–482, 1974.

Huyer, A., Coastal upwelling in the California Current system, *Prog. Oceanogr.*, *12*, 259–284, 1983.

Ikeda, M., and W. J. Emery, Satellite observations and modeling of meanders in the California Current system off Oregon and northern California, *J. Phys. Oceanogr.*, *14*, 1434–1450, 1984.

Johannessen, J. A., E. Svendsen, S. Sandren, O. M. Johannessen, and K. Lygre, Three-dimensional structure of mesoscale eddies in the Norwegian Coastal Current, *J. Phys. Oceanogr.*, *19*, 3–19, 1989.

Killworth, P. D., Long-wave instability of an isolated front, *Geophys. Astrophys. Fluid Dyn.*, *25*, 235–258, 1983.

Killworth, P. D., N. Paldor, and M. E. Stern, Wave propagation and growth on a surface front in a two-layer geostrophic current, *J. Mar. Res., 42,* 761-785, 1984.

Kosro, P. M., et al., The structure of the transition zone between coastal waters and the open ocean off northern California, winter and spring 1987, *J. Geophys. Res., 96,* 14,707-14,730, 1991.

Luther, M. E., and J. M. Bane Jr., Mixed instabilities in the Gulf Stream over the continental slope, *J. Phys. Oceanogr., 15,* 3-23, 1985.

Lutjeharms, J. R. E., F. A. Shillington, and C. M. Duncombe Rae, Observations of extreme upwelling filaments in the southeast Atlantic Ocean, *Science, 253,* 774-776, 1991.

McCreary, J. P., Y. Fukamachi, and P. K. Kundu, A numerical investigation of jets and eddies near an eastern ocean boundary, *J. Geophys. Res., 96,* 2515-2534, 1991.

Moore, G. W. K., and W. R. Peltier, Cyclogenesis in frontal zones, *J. Atmos. Sci., 44,* 384-409, 1987.

Moore, G. W. K., and W. R. Peltier, Frontal cyclogenesis and the geostrophic momentum approximation, *Geophys. Astrophys. Fluid Dyn., 45,* 183-197, 1989.

Moum, J. N., D. R. Caldwell, and P. J. Stabeno, Mixing and intrusions in a rotating cold-core feature off Cape Blanco, Oregon, *J. Phys. Oceanogr., 18,* 823-833, 1988.

Nakamura, N., Scale selection of baroclinic instability – Effects of stratification and nongeostrophy, *J. Atmos. Sci., 45,* 3253-3267, 1988.

Paduan, J. D., and P. P. Niiler, A Lagrangian description of motion in northern California coastal transition filaments, *J. Geophys. Res., 95,* 18,095-18,110, 1990.

Paldor, N., and M. Ghil, Shortwave instabilities of coastal currents, *Geophys. Astrophys. Fluid Dyn., 58,* 225-241, 1991.

Pedlosky, J., *Geophysical Fluid Dynamics,* 710 pp., Springer-Verlag, New York, 1987.

Samelson, R. M., Linear instability of a mixed-layer front, *J. Geophys. Res., 98,* 10,195-10,204, 1993.

Stevens, D. E., and P. E. Ciesielski, Inertial instability of horizontally sheared flow away from the equator, *J. Atmos. Sci., 43,* 2845-2856, 1986.

Stone, P. H., On non-geostrophic baroclinic stability, *J. Atmos. Sci., 23,* 390-400, 1966.

Stone, P. H., On non-geostrophic baroclinic stability, II, *J. Atmos. Sci., 27,* 721-726, 1970.

Strub, P. T., P. M. Kosro, A. Huyer, and CTZ Collaborators, The nature of the cold filaments in the California Current system, *J. Geophys. Res., 96,* 14,743-14,768, 1991.

Swenson, M. S., P. P. Niiler, K. H. Brink, and M. R. Abbott, Drifter observations of a cold filament off Point Arena, California, in July 1988, *J. Geophys. Res., 97,* 3593-3610, 1992.

Xue, H., and G. Mellor, Instability of the Gulf Stream front in the South Atlantic Bight, *J. Phys. Oceanogr., 23,* 2326-2350, 1993.

J.A. Barth, College of Oceanic and Atmospheric Sciences, Oregon State University, Ocean Administration Building 104, Corvallis, OR 97331-5503.